Translational Research in Anatomy 44 (2026) 100499

Contents lists available at ScienceDirect

Translational Research in Anatomy

journal homepage: www.elsevier.com/locate/tria

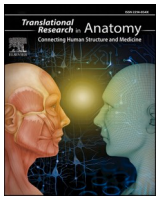

Preserved diffusion MRI measures despite subtle behavioral and hippocampal CA3 alterations in a preclinical model of cerebral small vessel disease

Che Mohd Nasril Che Mohd Nassir [a], Hafizah Abdul Hamid [b,*], Nurfatihah Pahdin [c], Izzatul Farhanis Abdul Halim [c], Laurasharwini Sivakumar [c], Mohd Khairi Hussain [c], Tengku Azam Shah Tengku Mohamad [c,**], Zaw Myo Hein [d], Muhammad Zulfadli Mehat [b]

[a] Department of Anatomy and Physiology, School of Basic Medical Sciences, Faculty of Medicine, Universiti Sultan Zainal Abidin, Kuala Terengganu, Terengganu, 20400, Malaysia
[b] Department of Human Anatomy, Faculty of Medicine and Health Sciences, Universiti Putra Malaysia, Serdang, Selangor, 43400, Malaysia
[c] Department of Biomedical Sciences, Faculty of Medicine and Health Sciences, Universiti Putra Malaysia, Serdang, Selangor, 43400, Malaysia
[d] Department of Basic Medical Sciences, College of Medicine, Ajman University, P.O.BOX:346, Ajman, United Arab Emirates

ARTICLE INFO

Keywords:
Cerebral small vessel disease
SHRSP
Diffusion tensor imaging
Hippocampus
CA3 vulnerability
Cognitive impairment
Microvascular dysfunction
Connectome
Preclinical model

ABSTRACT

Background: Cerebral small vessel disease (CSVD) is a major cause of vascular cognitive impairment, yet early-stage alterations remain insufficiently characterized. This study investigated the relationship between behavioral deficits, hippocampal microstructure, and histopathological changes in a preclinical CSVD model.
Methods: Male stroke-prone spontaneously hypertensive rats (SHRSP) and Wistar Kyoto (WKY) controls were evaluated at 8, 14, and 42 weeks. Behavioral assessments included open field, novel object recognition, and Morris's water maze. Brain MRI was performed using a 3.0 T system with diffusion tensor imaging (DTI), followed by region-of-interest analysis of the hippocampus. Histological evaluation included hematoxylin and eosin (H&E) and Nissl staining.
Results: SHRSP demonstrated age-associated behavioral alterations, including reduced locomotor activity (strain × age: $p = 0.013$), preserved recognition memory at early stages but declined at 42 weeks, and impaired spatial learning with absent acquisition improvement in aged animals. Notably, hippocampal DTI metrics remained unchanged across the examined experimental time points, with no significant effects of strain or age on fractional anisotropy (FA), mean diffusivity (MD), axial diffusivity (AD), or radial diffusivity (RD) (all $p > 0.25$). Whole-brain analyses yielded non-significant findings similarly. Histologically, enlarged perivascular spaces (ePVS) were consistently observed, while microbleeds and hemosiderin deposition were absent. Hippocampal thickness (CA1, CA3, dentate gyrus) was preserved; however, selective neuronal loss was detected in the CA3 subfield of aged SHRSP (42 weeks).
Conclusion: Behavioral decline was observed despite the absence of detectable hippocampal microstructural alterations using conventional DTI metrics, suggesting that functional impairment may emerge before abnormalities become evident within the sensitivity limits of the current imaging framework. These findings suggest that early CSVD involves subtle cellular and vascular dysfunction not captured by standard imaging, emphasizing the need for more sensitive, network-based, and molecular approaches.

This article is part of a special issue entitled: Clinical neuroanatomy and neuroscience published in Translational Research in Anatomy.

* Corresponding author.
** Corresponding author.
E-mail addresses: nasrilnassir@unisza.edu.my (C.M.N. Che Mohd Nassir), a_hafizah@upm.edu.my (H. Abdul Hamid), nrfthh143@gmail.com (N. Pahdin), izzatulfarhanis00@gmail.com (I.F. Abdul Halim), laurakumar65@gmail.com (L. Sivakumar), khairi@upm.edu.my (M.K. Hussain), azamshah@upm.edu.my (T.A.S. Tengku Mohamad), z.hein@ajman.ac.ae (Z.M. Hein), m_zulfadli@upm.edu.my (M.Z. Mehat).

https://doi.org/10.1016/j.tria.2026.100499
Received 1 May 2026; Received in revised form 18 May 2026; Accepted 26 May 2026
Available online 27 May 2026

1. Introduction

Cerebral small vessel disease (CSVD) is a major contributor to stroke and vascular cognitive impairment, yet its early pathogenesis remains poorly defined [1]. Although clinical studies have traditionally relied on overt neuroimaging features such as white matter hyperintensities (WMHs), lacunes, and microbleeds, these markers represent relatively advanced stages of disease [2,3]. Increasing evidence indicates that CSVD is fundamentally a disorder of the cerebral microvasculature, characterized by progressive structural alterations including arteriolosclerosis, vessel wall thickening, luminal narrowing, fibrinoid degeneration, and perivascular space enlargement [3,4]. These vascular changes impair cerebral perfusion and disrupt tissue homeostasis long before radiologically detectable lesions emerge [5], highlighting a critical need for experimental models that enable investigation of early-stage disease under controlled conditions.

Preclinical models have become indispensable for dissecting the temporal evolution of CSVD. Among these, the spontaneously hypertensive stroke-prone rats (SHRSP) are widely regarded as one of the most robust models, as it recapitulates key features of human CSVD, including chronic hypertension-induced vascular remodeling, endothelial injury, blood–brain barrier (BBB) disruption, and progressive microvascular rarefaction [6,7]. Structural alterations such as thickened vessel walls, reduced lumen diameter, microbleed formation, and hemosiderin deposition have been consistently observed in this model [8,9]. In contrast, Wistar Kyoto (WKY) rats serve as normotensive controls, providing a critical comparative framework for isolating disease-specific vascular and parenchymal changes. Importantly, the SHRSP model enables the study of early vascular pathology prior to overt stroke or extensive white matter damage, offering a unique window into the initial stages of CSVD progression.

Despite the availability of such models, a major limitation in the current preclinical literature is the fragmented evaluation of CSVD-related outcomes. Behavioral studies frequently report impairments in locomotor activity, exploratory behavior, and memory; however, these findings are often interpreted in isolation, without direct correlation to underlying vascular and structural alterations. Similarly, histopathological investigations have demonstrated vascular remodeling, perivascular space enlargement, microhemorrhages, and neuronal loss, yet many studies lack region-specific quantification within vulnerable brain structures such as the hippocampus [10]. This is particularly important given the functional heterogeneity of hippocampal subregions such as Cornu ammonis 1 (CA1), CA3, and dentate gyrus (DG), which are differentially susceptible to hypoperfusion and vascular insufficiency [11].

In parallel, neuroimaging approaches in preclinical CSVD research remain underutilized, particularly in linking microvascular pathology to tissue-level microstructural disruption and functional outcomes. Diffusion tensor imaging (DTI) has emerged as a sensitive modality for detecting early alterations in tissue organization, providing quantitative metrics such as fractional anisotropy (FA) and diffusivity indices that reflect axonal integrity, cellular density, and extracellular space changes [12]. In the context of CSVD, these alterations may arise secondary to chronic hypoperfusion, vascular stiffness, and impaired interstitial fluid dynamics [13]. When applied to hippocampal regions of interest (ROI), DTI tractography may offer the potential to capture early microstructural consequences of vascular dysfunction that are not detectable using conventional imaging. However, few studies have systematically integrated DTI-derived metrics with detailed vascular histopathology and behavioral assessment within the same experimental framework [14,15].

Furthermore, the hippocampus represents a critical nexus for investigating early CSVD-related dysfunction due to its high metabolic demand and vulnerability to microvascular compromise [16]. Vascular structural changes, including reduced capillary density, vessel wall thickening, and perivascular space dilation, may disrupt oxygen and nutrient delivery, leading to neuronal injury and synaptic dysfunction [16]. These processes are likely to manifest as subtle impairments in spatial learning, memory consolidation, and exploratory behavior, even in the absence of overt lesions [17]. Therefore, a comprehensive, multimodal approach is required to elucidate how vascular pathology drives microstructural brain alterations and subsequent cognitive deficits across disease progression.

In this context, the present study utilized SHRSP and WKY rat models to investigate early-stage CSVD through an integrated preclinical framework. Behavioral assessments, including the novel object recognition (NOR) and Morris's water maze (MWM), are combined with detailed histological evaluation of vascular and hippocampal structural changes using hematoxylin & eosin (H&E) and Nissl staining, and hippocampal DTI tractography. By examining age-dependent changes across these domains, this study aims to establish mechanistic links between vascular remodeling, neuronal integrity, microstructural disruption, and behavioral dysfunction, thereby providing a more comprehensive understanding of early CSVD progression.

2. Methodology

2.1. Study design, sample size determination, and animal allocation

All experimental procedures were carried out in compliance with the Institutional Animal Care and Use Committee (IACUC) guidelines of Universiti Putra Malaysia (UPM) and were approved under protocol number UPM/IACUC/AUP-R004/2021. The study was conducted at the Animal Behavioral Laboratory, Department of Human Anatomy, Faculty of Medicine and Health Sciences, UPM. Sample size estimation was performed a priori using parameters appropriate for a two-way analysis of variance (ANOVA), assuming a medium effect size ($f = 0.25$), a significance level of 0.05, and statistical power of 80%. Based on these assumptions, a minimum of 80 animals was required. To mitigate potential losses due to mortality, experimental exclusion, or imaging artifacts, an additional 20% was included, resulting in a target sample size of approximately 100 animals.

A total of 100 male rats (50 SHRSP and 50 WKY rats), aged 3 weeks, were obtained from the Animal Research and Service Centre, Universiti Sains Malaysia. Following a two-week acclimatization period, animals were randomly assigned to experimental groups based on a 2×3 factorial design, incorporating strain (SHRSP vs. WKY) and age as the main factors. The age variable consisted of three experimental time points selected to examine age-associated alterations within the SHRSP model: 8 weeks (pre-hypertensive phase), 14 weeks (established hypertension), and 42 weeks (stroke-prone phase). This design yielded six experimental groups (WKY and SHRSP at 8, 14, and 42 weeks), with approximately 16–17 animals per group to ensure balanced group sizes. This factorial framework enabled the evaluation of both independent and interaction effects of strain and age on all measured outcomes. A schematic overview of the study design is presented in Fig. 1. Throughout the experimental period, animals were housed in groups of two to three per cage under standardized laboratory conditions (temperature: $22 \pm 2\ ^{\circ}C$; relative humidity: 50–60%) with a 12-h light–dark cycle. Food and water were provided ad libitum.

2.2. Vascular risk factors

Body weight and systolic blood pressure (SBP) were recorded longitudinally in all animals ($n = 100$) on a weekly basis following a two-week acclimation period. Body weight was measured using a calibrated digital balance under standardized conditions to ensure consistency across time points. SBP was measured non-invasively using a tail-cuff system (CODA®, Kent Scientific Corporation, USA), a validated method for serial blood pressure monitoring in conscious rodents. To reduce stress-related variability, animals were subjected to a habituation phase prior to data acquisition, which involved repeated exposure to

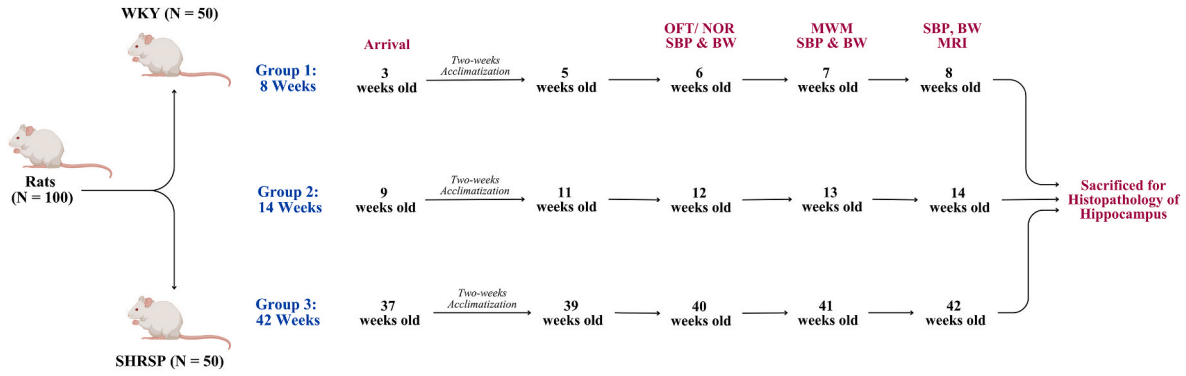

Fig. 1. A schematic overview of the study design.

restraint and the tail-cuff apparatus over several days.

All recordings were performed in a controlled environment with ambient temperature maintained at approximately 30–32 °C to promote adequate tail perfusion. Measurements were conducted at a fixed time of day to minimize circadian influences. For each session, a series of consecutive readings (typically 5–10 cycles) was obtained, and only stable, artifact-free measurements were included in the analysis. The average of the accepted cycles was used to represent SBP at each time point. In cases where excessive movement or signal inconsistency was observed, measurements were repeated to ensure data quality and reliability.

2.3. Behavioral assessments

2.3.1. Open field test (OFT)

The OFT was used to assess spontaneous locomotor activity, exploratory behavior, and anxiety-related responses in rodents. The test was conducted in a square Plexiglas arena (75 × 75 × 40 cm) with the

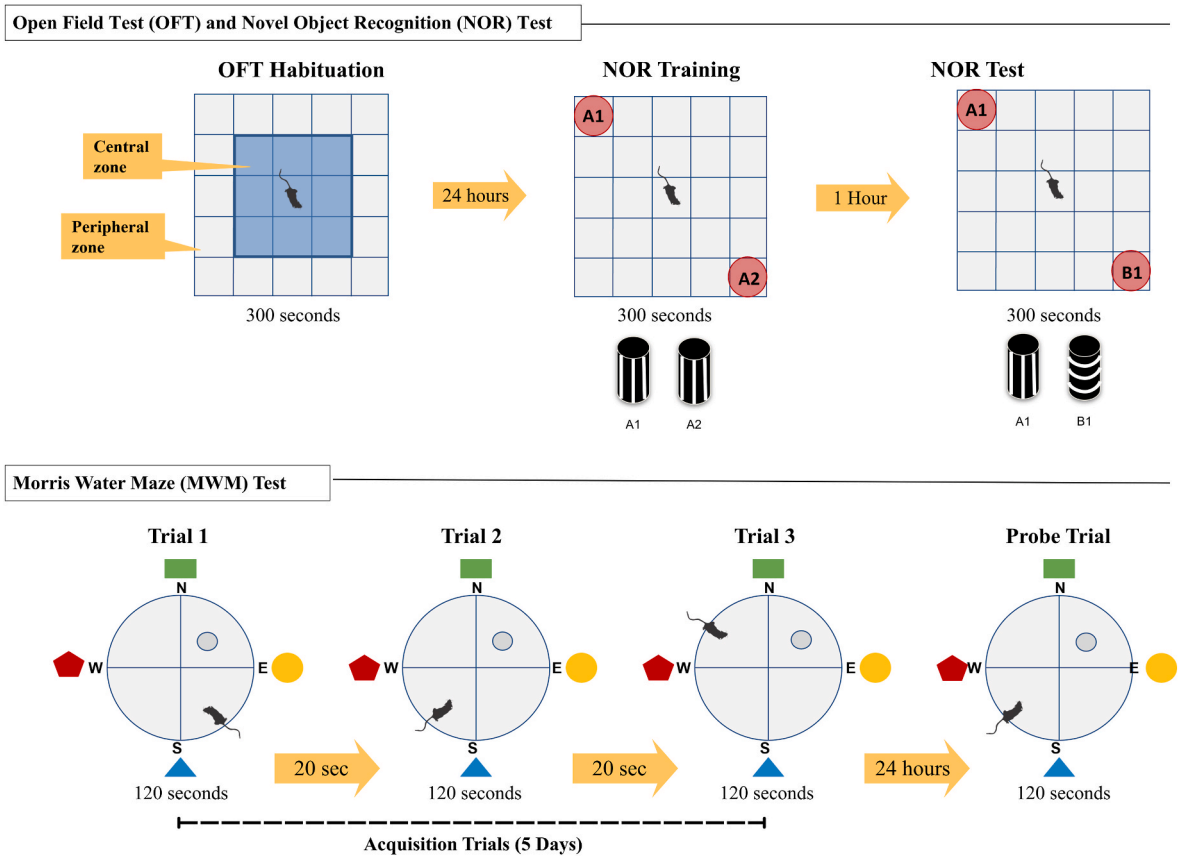

Fig. 2. Experimental timelines and schematics of behavioral testing procedures. This figure illustrates the protocols for evaluating exploratory behavior, memory, and spatial navigation. Open Field Test (OFT) and Novel Object Recognition (NOR) Test: The OFT habituation phase allows for the assessment of baseline locomotor activity and anxiety-like behavior by monitoring exploration of the Central zone versus the Peripheral zone over 300 s. Following a 24-h interval, the NOR training phase familiarizes the subject with two identical objects (A1 and A2) for 300 s. After a 1-h delay, the NOR test phase assesses short-term recognition memory by introducing a novel object (B1) alongside a familiar object (A1). Increased interaction with B1 indicates intact memory. Morris's Water Maze (MWM) Test: This paradigm assesses spatial learning and reference memory. During the acquisition trials (conducted over 5 days), subjects are trained to locate a hidden platform within a circular pool. Each trial lasts up to 120 s, with short inter-trial intervals (e.g., 20 s). Visual cues (depicted as symbols at the cardinal points) assist in spatial navigation. Finally, a Probe Trial, conducted 24 h after the last acquisition trial, evaluates memory retention by removing the platform to measure the subject's preference for the target quadrant where the platform was previously located.

floor demarcated into 25 equal squares to facilitate behavioral quantification (Fig. 2). Following brief acclimatization to the testing environment, each rat was placed in the center of the arena and allowed to explore freely for 5 min. After each trial, the apparatus was cleaned thoroughly using 70% ethanol to remove any olfactory traces and prevent cue-based bias. Behavioral activity was recorded using an overhead camera connected to an automated tracking system (ANY-maze, version 7.44, USA). The software was used to extract locomotor parameters, including total distance travelled, number of line crossings, and movement velocity. The protocol was adapted from previously described methods [18,19].

2.3.2. Novel object recognition (NOR)

Recognition memory was evaluated using the NOR paradigm, which exploits the natural tendency of rodents to preferentially investigate unfamiliar objects. The procedure was adapted from previously established protocols with minor adjustments [20]. Testing was conducted in a square Plexiglas arena measuring 75 × 75 × 40 cm. The objects used were constructed from plastic and differed in geometry (e.g., cylindrical versus cuboidal) while maintaining comparable size (approximately 10–12 cm in height) (Fig. 2). Prior to testing, animals were acclimated to the empty arena for 5 min on the day preceding the experiment. The task consisted of two phases: acquisition and retention.

During the acquisition phase, each rat was placed in the arena containing two identical objects and allowed to explore freely for 5 min. After a 30-min interval, the retention phase was carried out, during which one of the previously encountered objects was substituted with a novel object. Rats were again given 5 min to explore. To prevent spatial preference from influencing the results, the position of the novel object was systematically alternated across trials. Exploratory behavior was defined as active interaction with the object, including directing the snout toward it within a distance of approximately 2 cm, as well as sniffing or physical contact using the forelimbs. Passive proximity without directed attention was not considered exploration. The duration of exploration for each object was manually recorded in seconds.

Data analysis focused on the retention phase. The following parameters were derived: (i) time spent investigating the familiar object (A1), (ii) time spent investigating the novel object (B1), and (iii) total exploration time (e2), calculated as the sum of A1 and B1. Recognition memory performance was quantified using the discrimination index (DI) and recognition index (RI), calculated as:

$$DI = \frac{B1 - A1}{B1 + A1}$$

$$RI = \frac{A1}{e2} \times 100\%$$

These indices reflect the relative preference for novelty, with higher values indicating better recognition memory. Although additional variables, including acquisition-phase exploration and absolute discrimination (d1), were recorded, only DI and RI are reported to maintain clarity and emphasize key outcomes.

2.3.3. Morris Water Maze (MWM)

Spatial learning and memory were assessed using the MWM paradigm (Fig. 2). The apparatus consisted of a circular tank (122 cm diameter, 62.5 cm height) filled with water made opaque using non-toxic white coloring. The pool was conceptually partitioned into four equal quadrants, with a hidden escape platform (10 cm in diameter) positioned in the northeast (NE) quadrant. The platform was submerged approximately 2 cm below the water surface to prevent visual detection. All trials were conducted under controlled, low-light conditions using dim halogen illumination to minimize external visual cues. Before the commencement of training, animals were subjected to a single 120-s pre-exposure swim to facilitate acclimatization to the testing environment and to identify any rats unable to perform the task.

The acquisition phase was carried out over five consecutive days, during which each animal completed three trials per day. At the start of each trial, rats were introduced into the pool from varying entry points in a pseudo-random sequence, excluding the quadrant containing the hidden platform. Each trial lasted a maximum of 120 s. Upon locating the platform, animals were allowed to remain on it for 20 s. If a rat failed to find the platform within the allotted time, it was gently guided to the platform and permitted the same rest period.

Performance during acquisition was quantified using escape latency and swim distance, both recorded via an automated tracking system (ANY-maze, version 7.44, USA). To evaluate memory retention, a probe trial was conducted on day six. In this session, the escape platform was removed, and each rat was released from the quadrant opposite the original platform location. The time spent in the target (NE) quadrant was recorded over a 30-s interval and used as an indicator of spatial memory retention.

2.4. Magnetic resonance imaging (MRI)

2.4.1. Image acquisition

MRI was performed using a 3.0 Tesla clinical scanner (MAGNETOM Prisma, Siemens Healthineers, Germany) configured for small-animal imaging. Anesthesia was induced with 3–4% isoflurane in oxygen and maintained at 1.5–2.0% via a nose cone throughout the scanning session. To reduce motion-related artifacts, the head of each animal was carefully secured using a dedicated fixation setup.

2.4.2. Structural imaging

High-resolution anatomical datasets were acquired using three-dimensional T1-weighted magnetization-prepared rapid gradient echo (MPRAGE) and T2-weighted SPACE sequences. For T1-weighted imaging, acquisition parameters included: repetition time (TR) = 1170 ms, echo time (TE) = 5.66 ms, field of view (FOV) = 50 mm, matrix size corresponding to a base resolution of 256, slice thickness = 0.5 mm, and a voxel dimension of 0.2 × 0.2 × 0.5 mm. The total scan duration was approximately 18 min and 35 s. T2-weighted images were obtained using a SPACE sequence with TR = 2500 ms and TE = 351 ms. Imaging was performed with an FOV of 50 mm, base resolution of 128, slice thickness of 0.3 mm, and voxel size of 0.2 × 0.2 × 0.3 mm, yielding a total acquisition time of 17 min and 54 s. No exogenous contrast agents were used.

2.4.3. Diffusion tensor imaging (DTI)

DTI was conducted to characterize brain microstructure using a diffusion-weighted spin-echo echo-planar imaging (EPI) sequence. The acquisition parameters were as follows: TR = 5100 ms, TE = 99 ms, FOV = 40 mm, slice thickness = 1.0 mm, base resolution = 80, and voxel size of 0.3 × 0.3 × 1.0 mm. The total scan time for the diffusion protocol was 17 min and 26 s. From the diffusion datasets, quantitative maps were generated, including fractional anisotropy (FA), mean diffusivity (MD), axial diffusivity (AD), and radial diffusivity (RD). Directionally encoded color FA maps were also produced to visualize fiber orientation by integrating eigenvector directionality with anisotropy magnitude.

2.4.4. Diffusion reconstruction and tractography

Post-processing of diffusion data, including reconstruction and tractography, was performed using DSI Studio (Yeh, 2025; Hou "侯" version, February 10, 2026; http://dsi-studio.labsolver.org) [21]. Tensor reconstruction was applied to derive diffusion metrics and facilitate fiber tracking. Whole-brain tractography was generated using a deterministic streamline approach. The acquisition followed a high-angular resolution diffusion imaging (HARDI) scheme with 200 sampling directions and a *b*-value of 1000 s/mm^2. Imaging resolution included an in-plane voxel size of 0.250 mm and a slice thickness of 1.00 mm. Signal inhomogeneity was corrected using the b0 reference image.

Fiber tracking was performed using a deterministic algorithm with enhanced propagation strategies to improve reproducibility [22]. The angular threshold ranged between 45° and 90°, and the step size corresponded to voxel spacing. Streamlines shorter than 10 mm or exceeding 40 mm were excluded to reduce spurious tracts. A total of 1,000,000 seeds were distributed across the brain volume. Shape-based metrics were also derived to characterize tract geometry. All tracking parameters were held constant across subjects to ensure comparability between experimental groups. Region-specific analyses were conducted using anatomically defined ROIs, i.e., the hippocampus derived from the Duke Center for In Vivo Microscopy (DukeCIVM) rat brain atlas integrated within DSI Studio. The diffusion-derived metrics (FA, MD, AD, and RD) were extracted to quantify microstructural integrity and enable comparison across experimental groups.

2.5. Histology: Brain isolation and fixation

At the designated experimental endpoints (after MRI scanning), animals were euthanized according to their respective age groups (8-week group at week 9, 14-week group at week 15, and 42-week group at week 43). Prior to tissue collection, the rats were deeply anesthetized using inhalational isoflurane to achieve a surgical plane of anesthesia, ensuring the absence of reflexes and minimizing distress. Following confirmation of adequate anesthesia, cardiac puncture was performed to collect blood samples for downstream analyses. Subsequently, animals were euthanized, and the brains were rapidly extracted through careful dissection of the skull to avoid mechanical damage to the tissue.

Immediately after removal, whole brains were immersed in 10% neutral buffered formalin for fixation. The fixation process was carried out for a minimum of 48 h to ensure thorough penetration of the fixative and optimal preservation of cellular morphology and tissue architecture. This step is critical for maintaining structural integrity and preventing post-mortem degradation prior to histological processing. Additional organs and tissues were also collected and appropriately preserved for future analytical purposes or ancillary studies. All remaining carcasses and biological waste were handled and disposed of in accordance with institutional biosafety and animal ethics guidelines, ensuring compliance with approved IACUC protocols and standard laboratory safety regulations.

2.6. Hematoxylin and eosin (H&E) and Nissl staining

Brains were coronally sectioned, placed in labeled cassettes, and returned to 10% neutral buffered formalin prior to processing. Tissue processing was performed using an automated tissue processor (~15 h). Samples underwent graded dehydration in ethanol (70%, 95%, and 100%), followed by clearing in xylene and paraffin infiltration. Following processing, tissues were embedded in paraffin using a Leica embedding system. Samples were oriented in molds, infiltrated with molten paraffin, and solidified on a cold plate to form paraffin blocks. Blocks were stored at room temperature until sectioning. Paraffin blocks were trimmed and sectioned using a Leica microtome at a thickness of 5 μm. Sections were floated on a 37 °C water bath and mounted onto glass slides. Slides were air-dried at room temperature for 2–3 days prior to staining.

H&E staining was performed using an automated Leica Autostainer (~2 h). Sections were deparaffinized in xylene, rehydrated through graded alcohol, and stained with hematoxylin followed by eosin. Slides were then dehydrated, cleared, and coverslipped. This staining enabled evaluation of hippocampal cytoarchitecture and identification of pathological features. H&E-stained sections were examined under a light microscope (40× magnification) to identify vascular and structural abnormalities, including microbleeds, hemosiderin deposition, vessel wall thickening, and enlarged perivascular spaces. Observations were recorded across the entire hippocampal region and interpreted based on established morphological criteria. Additionally, hippocampal thickness was measured using an image analysis system coupled with a light microscope. Subregions (CA1, CA3, and DG) were assessed at 20× magnification. Five measurements per region were obtained per sample, and mean values were calculated for analysis.

Neuronal integrity was assessed using cresyl violet (Nissl) staining. Sections mounted on Superfrost Plus slides were deparaffinized, rehydrated, and stained with 0.1% cresyl violet solutions. After staining, sections were rinsed, differentiated in graded alcohol, cleared in xylene, and cover-slipped. The procedure was completed within approximately 50 min. Nissl-stained sections were imaged at 40× magnification. Six fields from each hippocampal subregion (CA1, CA3, and DG) were captured. Images were analyzed using ImageJ software to quantify viable and non-viable neurons. Cell viability was calculated as:

$$\text{Cell viability } (\%) = \frac{\text{Number of viable cells} - \text{Number of dead cells}}{\text{Total number of cells}} \times 100\%$$

All histological and image-based analyses were performed under blinded conditions. Slides were coded by an independent researcher to conceal group allocation (strain and age) from the evaluators. Quantification of hippocampal thickness and neuronal counts was conducted independently by two trained observers. Inter-rater reliability was assessed using the intraclass correlation coefficient (ICC) based on a two-way random-effects model with absolute agreement. Inter-rater agreement demonstrated excellent reliability across all hippocampal subregions (CA1: ICC = 0.93, 95% CI [0.88–0.96]; CA3: ICC = 0.91, 95% CI [0.85–0.95]; DG: ICC = 0.94, 95% CI [0.90–0.97]). Neuronal counts from Nissl-stained sections similarly showed high reproducibility (ICC = 0.92, 95% CI [0.87–0.96]). ICC values > 0.75 were considered indicative of good reliability, while values > 0.90 reflected excellent agreement.

For measurements with discrepancies exceeding 10% between observers, a joint review was performed to reach consensus. Intra-rater reliability was evaluated by re-analyzing approximately 20% of samples after a two-week interval, demonstrating excellent consistency (ICC >0.90 across all parameters). All image analyses were performed using standardized acquisition settings and calibration parameters to ensure consistency across samples. These procedures minimized observer bias and enhanced the reproducibility of quantitative measurements.

2.7. Statistical analysis

All statistical analyses were performed using IBM Statistical Package for the Social Sciences (SPSS, version 29.0, IBM Corp., Armonk, NY, USA). Data are presented as mean ± standard deviation (SD). Between-group comparisons were conducted using two-way analysis of variance (ANOVA) to evaluate the main effects of strain (SHRSP vs. WKY), age (8, 14, and 42 weeks), and their interaction. For behavioral measures involving repeated testing (e.g., Morris Water Maze acquisition trials), a two-way repeated-measures ANOVA was applied, with time/trial as the within-subject factor. When significant main or interaction effects were observed, Bonferroni-adjusted post hoc tests were performed for multiple comparisons. Assumptions of normality and homogeneity of variance were assessed prior to analysis. A *p*-value of less than 0.05 was considered statistically significant.

3. Results

A total of 100 male rats (50 SHRSP and 50 WKY) were recruited at the start of the study. Over the course of the experiment, a small number of animals were lost due to spontaneous mortality and/or study-related factors. Such attrition is expected in longitudinal studies involving ageing and hypertensive models, particularly in the SHRSP strain. As a result, 93 animals remained available for final analysis. The distribution of animals across groups was as follows: WKY: 8 weeks (n = 15), 14

weeks (n = 15), and 42 weeks (n = 17); SHRSP: 8 weeks (n = 15), 14 weeks (n = 15), and 42 weeks (n = 16). Despite this limited loss, group sizes remained well balanced, supporting reliable statistical comparisons for both strain and age effects. All animals were housed and maintained under standardized conditions as previously described.

3.1. Validation of CSVD model: vascular risk profile

The systolic blood pressure (SBP) and body weight were analyzed across strain (WKY vs SHRSP) and age (8, 14, and 42 weeks) using two-way ANOVA (Table 1). For SBP, a significant main effect of strain was observed ($p = 0.017$), indicating consistently higher blood pressure in SHRSP rats compared to WKY controls across the study period. However, neither the main effect of age ($p = 0.405$) nor the strain × age interaction ($p = 0.477$) reached statistical significance, suggesting that temporal SBP changes within the present dataset should be interpreted cautiously and do not independently establish progressive vascular worsening across age groups based solely on the current physiological measurements. Descriptively, WKY rats showed a modest increase in SBP from 8 weeks to 14 weeks, followed by a slight decline at 42 weeks. Similarly, SHRSP rats exhibited persistently elevated SBP across all examined age groups, consistent with the established hypertensive phenotype of this strain, although age-dependent progression within the present dataset was not statistically significant. Nevertheless, within-strain comparisons using one-way ANOVA did not reveal statistically significant differences across age points ($p > 0.05$) (Fig. 3A).

In contrast, body weight was significantly influenced by both strain and age. Two-way ANOVA revealed significant main effects of strain ($p < 0.001$) and age ($p < 0.001$), as well as a significant strain × age interaction ($p = 0.001$). Overall, WKY rats displayed higher body weight compared to SHRSP rats at all time points, with both groups exhibiting progressive weight gain over time. The increase was more pronounced in WKY rats, particularly at 42 weeks (Fig. 3B). Post hoc analysis further confirmed significant age-dependent increases in body weight within each strain, with all pairwise comparisons (8 vs 14 weeks, 14 vs 42 weeks, and 8 vs 42 weeks) reaching statistical significance (all $p < 0.001$), indicating a consistent growth trajectory across both experimental groups.

Table 1
Effects of strain and age on systolic blood pressure (SBP) and body weight (N = 93).

Variable	Group	Age	Mean ± SD	n
SBP (mmHg)	WKY	8W	99.62 ± 21.31	15
		14W	117.95 ± 25.70	15
		42W	112.18 ± 49.64	17
	SHRSP	8W	125.95 ± 20.70	15
		14W	123.78 ± 35.43	15
		42W	140.44 ± 62.79	16
	Strain effect, (F [1,8] = 5.943, $p = 0.017$, partial $\eta^2 = 0.064$)			
	Age effect, (F[2,87] = 0.913, $p = 0.405$, partial $\eta^2 = 0.021$)			
	Strain × Age, (F[2,87] = 0.747, $p = 0.477$, partial $\eta^2 = 0.017$)			
Body weight (g)	WKY	8W	215.13 ± 34.53	15
		14W	349.53 ± 45.92	15
		42W	482.41 ± 60.59	17
	SHRSP	8W	178.20 ± 18.71	15
		14W	279.13 ± 49.95	15
		42W	346.94 ± 77.15	16
	Strain effect, (F[1,87] = 56.58, $p < 0.001$, partial $\eta^2 = 0.394$)			
	Age effect, (F[2,87] = 138.80, $p < 0.001$, partial $\eta^2 = 0.761$)			
	Strain × Age, (F[2,87] = 7.40, $p = 0.001$, partial $\eta^2 = 0.145$)			

Data are presented as mean ± standard deviation (SD). Statistical analysis was performed using two-way analysis of variance (ANOVA) with strain and age as independent factors. The interaction term represents the combined effect of strain and age (strain × age). Partial η^2 (eta squared) indicates effect size, interpreted as small (≥0.01), medium (≥0.06), and large (≥0.14). Homogeneity of variance was assessed using Levene's test, which indicated significant heterogeneity for both SBP ($p < 0.001$) and body weight ($p = 0.001$). Therefore, results should be interpreted with caution. A p-value <0.05 was considered statistically significant. Sample sizes (n) represent the number of animals per group. WKY, Wistar Kyoto rats; SHRSP, Stroke-prone spontaneously hypertensive rats; SBP, Systolic blood pressure.

3.2. OFT: locomotor activity and exploratory behavior

Locomotor activity, quantified by total distance travelled, was analyzed using two-way ANOVA to assess the effects of strain and age (Fig. 3C). A significant interaction between strain and age was observed (F [2,23] = 4.676, $p = 0.013$), indicating that age-related changes in activity differed between SHRSP and WKY rats. Post hoc analysis (Bonferroni correction) revealed that SHRSP rats exhibited a significant reduction in locomotor activity at 14 weeks ($p = 0.024$) and 42 weeks ($p < 0.001$) compared to their 8-week counterparts. Although a further decline was noted at 42 weeks relative to 14 weeks, this difference did not reach statistical significance. In contrast, WKY rats showed no significant age-dependent changes in locomotor activity. Between-group comparisons indicated lower locomotor activity in SHRSP rats at both 14 and 42 weeks; however, statistical significance was reached only at 42 weeks ($p = 0.011$). Overall, older SHRSP rats demonstrated reduced locomotor activity relative to earlier ages, representing the clearest statistically supported behavioral alteration observed in the present study.

Time allocation in the central and peripheral zones was further analyzed to evaluate exploratory behavior. At 8 weeks, no significant interaction between strain and zone was detected (F [1,24] = 1.620, $p = 0.211$) (Fig. 3D). Both strains spent significantly more time in the peripheral zone compared to the central zone (F [1,24] = 172.6, $p < 0.001$), reflecting a strong preference for the periphery. Although SHRSP rats showed a trend toward increased peripheral occupancy relative to WKY rats, this difference was not statistically significant. At 14 weeks, a significant strain × zone interaction was observed (F [1, 25] = 15.23, $p < 0.001$] (Fig. 3E). Post hoc analysis confirmed that both groups preferred the peripheral zone over the central zone ($p < 0.001$). Notably, SHRSP rats exhibited altered exploratory patterns, characterized by increased time spent in the central zone and reduced peripheral preference compared to WKY rats ($p = 0.018$), suggesting changes in exploration strategy.

At 42 weeks, the interaction between strain and zone remained significant (F [1,26] = 7.190, $p = 0.011$) (Fig. 3F). Both SHRSP and WKY rats continued to spend more time in the peripheral zone than in the central zone ($p < 0.001$). Although SHRSP rats showed a tendency toward increased central exploration relative to WKY controls, this difference did not reach statistical significance. Overall, SHRSP rats demonstrated a shift in exploratory behavior with age, characterized by altered central–peripheral distribution and a general increase in central zone engagement compared to WKY rats across time points.

3.3. NOR: recognition memory

Recognition memory performance was evaluated using the DI, which reflects the ability to distinguish between novel and familiar objects. Positive values indicate a preference for the novel object, negative values indicate a preference for the familiar object, and values around zero reflect no clear preference. A two-way ANOVA followed by Bonferroni post hoc analysis was performed to examine the effects of strain and age on DI (Fig. 3G). No significant interaction between strain and age was observed (F[2, 68] = 1.257, $p = 0.291$).

In SHRSP rats, DI values remained positive at 8 weeks and 14 weeks, indicating preserved recognition memory during early and midlife (Table 2). However, at 42 weeks, SHRSP rats showed a marked reduction in performance, with DI approximating zero or slightly negative, suggesting loss of novelty discrimination ability. In contrast, WKY rats

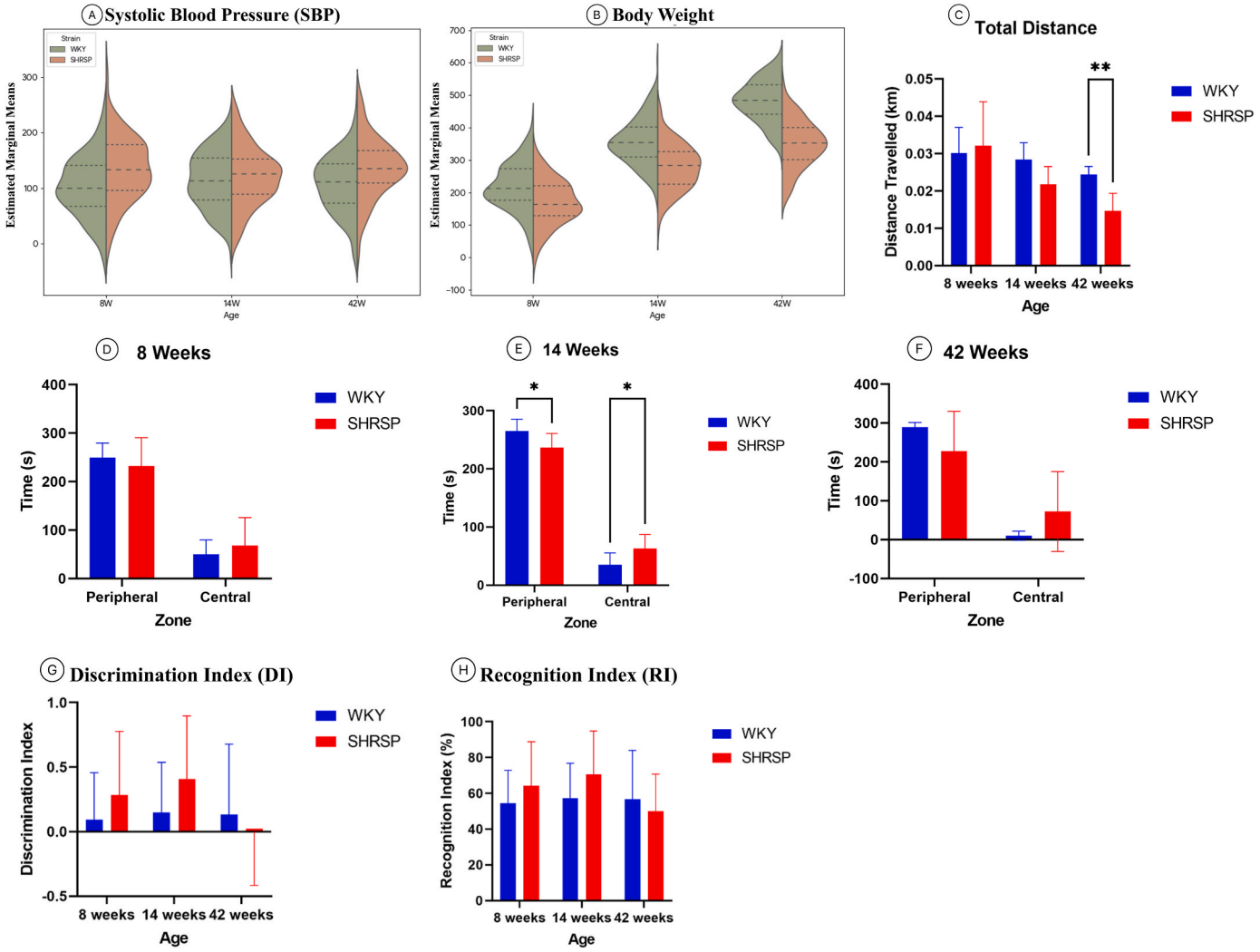

Fig. 3. Physiological and behavioral profiles of Wistar-Kyoto (WKY) and stroke-prone spontaneously hypertensive (SHRSP) rats across age groups. (A–B) Violin plots showing the distribution of systolic blood pressure (SBP) and body weight (BW) at 8, 14, and 42 weeks. (C) Total distance travelled in the open field test (OFT), demonstrating reduced locomotor activity in aged SHRSP rats. (D–F) Time spent in the peripheral and central zones of the OFT at 8, 14, and 42 weeks, indicating age- and strain-dependent anxiety-like behavior. (G–H) Cognitive performance was assessed via the discrimination index (DI) and recognition index (RI) during the novel object recognition (NOR) test, showing variability in recognition memory across cohorts. *Note: Data are expressed as mean ± standard deviation (SD). Statistical significance is indicated by $*p < 0.05$ and $*p < 0.01$.

maintained positive DI values across all age groups, reflecting stable recognition memory performance over time. Although SHRSP showed lower DI than WKY at 42 weeks, this difference was not statistically significant.

A similar pattern was observed for the RI, which represents the percentage preference for the novel object, with 50% indicating chance-level performance (Fig. 3H). Two-way ANOVA revealed no significant interaction between strain and age ($F[2, 68] = 1.265, p = 0.289$). SHRSP rats demonstrated clear novelty preference at 8 weeks and 14 weeks, with a peak at 14 weeks, but this preference was lost at 42 weeks, indicating impaired recognition performance at later stages. WKY rats consistently displayed novelty preference across all age groups, with only minor fluctuations over time. Between-group comparisons showed lower RI in SHRSP compared to WKY at 42 weeks; however, this difference did not reach statistical significance.

3.4. MWM: spatial learning and memory

At 8 weeks, no significant interaction between strain and acquisition day was observed ($F[4, 104] = 0.645$, $p = 0.632$), indicating similar learning trajectories in SHRSP and WKY rats (Fig. 4). A significant main effect of day was detected ($F[2.365, 61.50] = 11.52$, $p < 0.001$), reflecting progressive improvement in task performance across training sessions. However, no significant main effect of strain was found ($F[1, 27] = 2.778$, $p = 0.108$). Post hoc analysis revealed a reduction in escape latency across days in both groups, with WKY rats showing a significant improvement between day 2 and day 5 ($p = 0.002$), while SHRSP rats demonstrated significant reductions from day 1 to days 3, 4, and 5 (all $p \leq 0.007$) as well as between day 2 and day 3 ($p = 0.031$). Collectively, these findings indicate preserved spatial learning ability in both strains at this age.

At 14 weeks, no significant interaction between strain and training day was observed ($F[4, 92] = 0.777$, $p = 0.543$), and no significant main effect of strain was detected ($F[1,28] = 4.222$, $p = 0.051$), although a strong trend toward group differences was noted (Fig. 4). A significant effect of day was present ($F[2.044, 47.02] = 16.96$, $p < 0.001$), indicating learning across trials in both groups. Post hoc comparisons showed that WKY rats exhibited consistent improvement across multiple days, whereas SHRSP rats demonstrated fewer significant within-group reductions in escape latency, primarily at later training stages. Despite these differences in learning dynamics, both strains ultimately showed reduced latency over time, indicating overall preserved spatial learning

Table 2
Discrimination index (DI) and recognition index (RI) in WKY and SHRSP rats across age groups.

(A) Discrimination Index (DI)				
Strain	Age	Mean DI	SD	Interpretation
WKY	8 weeks	0.091	0.094	Novel preference (weak)
	14 weeks	0.146	0.104	Novel preference
	42 weeks	0.133	0.173	Novel preference
SHRSP	8 weeks	0.284	0.137	Preserved recognition
	14 weeks	0.410	0.147	Strong recognition
	42 weeks	−0.001	0.125	Impaired/no preference
(B) Recognition Index (RI, % novel object preference)				
Strain	Age	Mean RI (%)		Interpretation
WKY	8 weeks	54.513		Novel preference
	14 weeks	57.304		Novel preference
	42 weeks	56.589		Stable novelty preference
SHRSP	8 weeks	64.175		Strong novelty preference
	14 weeks	70.510		Peak performance
	42 weeks	49.968		Chance level/impaired

SD, standard deviation.

at this stage.

At 42 weeks, no significant interaction between strain and acquisition day was observed ($F[4, 76] = 1.644$, $p = 0.172$), nor were there significant main effects of strain ($F[1,19] = 1.197$, $p = 0.288$) or day ($F[2.381, 45.25] = 1.222$, $p = 0.309$) (Fig. 4). Post hoc analysis revealed significant reductions in escape latency in WKY rats between day 1 and day 4 and 5 ($p = 0.003$ and $p = 0.036$, respectively), indicating retained learning capacity. In contrast, aged SHRSP rats demonstrated less consistent improvement across acquisition days compared to WKY controls, suggesting possible vulnerability in spatial learning performance. However, several strain effects and probe-trial outcomes did not reach statistical significance, and therefore these findings should be interpreted cautiously.

Spatial memory was further evaluated using the percentage of time spent in the target quadrant during the probe trial (Fig. 4). Two-way ANOVA revealed no significant interaction between strain and age ($F[2, 68] = 0.630$, $p = 0.535$). In SHRSP rats, time spent in the target quadrant showed a gradual decline across age groups (8 weeks: 8.99%; 14 weeks: 6.56%; 42 weeks: 6.30%), although these changes were not statistically significant. WKY rats exhibited a similar non-significant pattern, with values of 7.45% (8 weeks), 5.80% (14 weeks), and 6.89% (42 weeks). Between-group comparison showed lower performance in SHRSP relative to WKY at 42 weeks; however, this difference did not reach statistical significance. Overall, probe trial performance suggests a trend toward age-associated decline in spatial memory, with more pronounced impairment emerging in SHRSP rats at later stages.

3.5. Histopathological findings

3.5.1. Vascular and structural abnormalities

Among the abnormalities evaluated, neither microbleeds nor hemosiderin deposition was detected in any group. In contrast, enlarged perivascular spaces (ePVS) were consistently observed across all strains and age groups (Fig. 5A–F), indicating a common structural feature within the hippocampal microenvironment. Vessel wall morphology demonstrated variability between groups. Thickened vessel walls were identified in both SHRSP and WKY rats, although their distribution differed across age groups (Fig. 5G–L). Notably, thick vessel walls were absent in the 14-week WKY group but present in the SHRSP group at all examined ages. Quantitative analysis (Fig. 5M) revealed no significant differences in the prevalence of vessel wall thickening across SHRSP age groups, nor between SHRSP and corresponding WKY controls. These findings suggest that, despite observable vascular alterations, the extent of vessel wall thickening does not differ significantly across disease stages in this model.

3.5.2. Hippocampal thickness

Morphometric analysis of hippocampal subregions (CA1, CA3, and

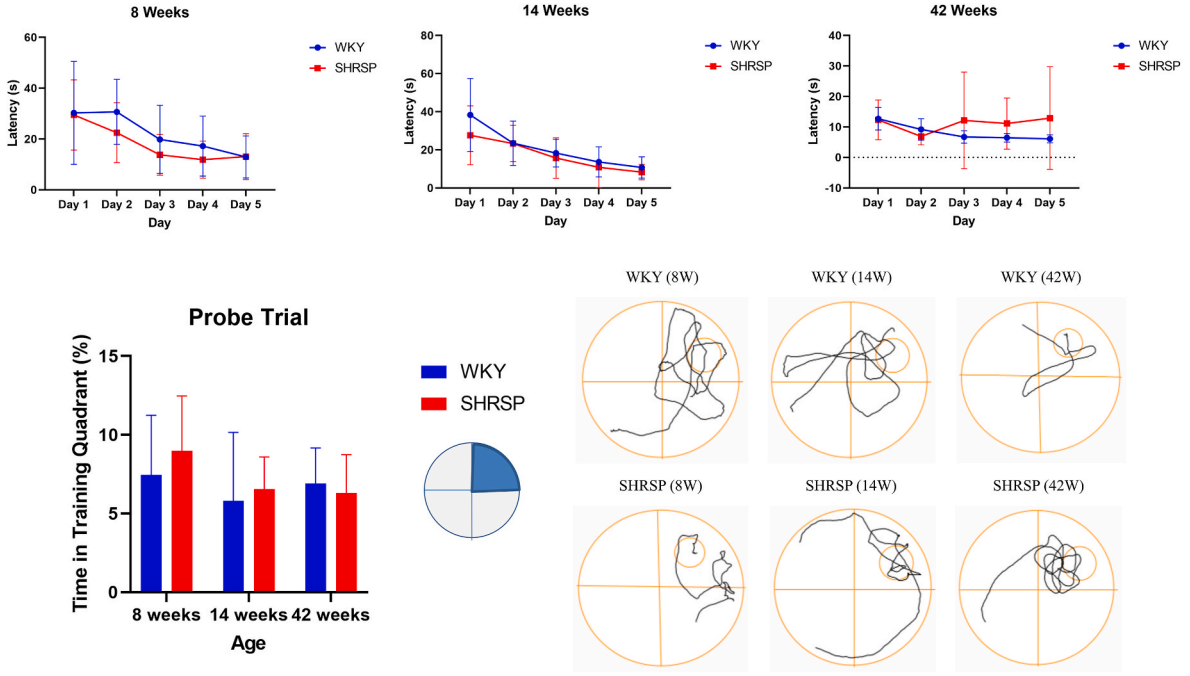

Fig. 4. Assessment of spatial learning and memory via Morris's water maze (MWM) performance among Wistar-Kyoto (WKY) and stroke-prone spontaneously hypertensive (SHRSP) rats. Top Panels (Latency): Learning curves depicting the mean latency to locate the hidden platform across 5 acquisition days for 8-, 14-, and 42-week-old cohorts. Bottom Left (Probe Trial): Time spent in the target quadrant during the memory retention probe trial, illustrating spatial reference memory. Bottom Right (Representative tracks): Sample swim paths for each group, visualizing search strategies and spatial bias toward the target location (indicated by the small circle).

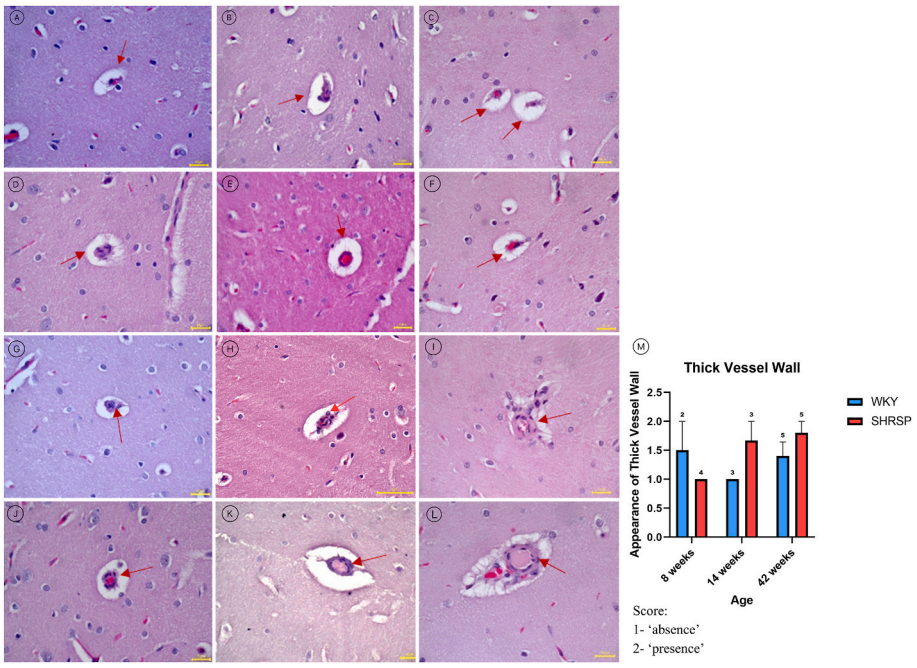

Fig. 5. Representative Hematoxylin and Eosin (H&E) staining of cerebral perivascular spaces and vascular wall morphology in Wistar-Kyoto (WKY) and spontaneous hypertensive stroke-prone (SHRSP) rats. Micrographs demonstrate structural changes across age cohorts (8, 14, and 42 weeks) at 40× magnification. (A–F) Enlarged perivascular spaces (ePVS): Longitudinal comparison showing the prominence of ePVS in the parenchyma of WKY (A-C: 8, 14, and 42 weeks respectively) and SHRSP (D-F: A-C, 8, 14, and 42 weeks respectively) rats. Red arrows indicate areas of perivascular widening. (G–L) Vascular wall morphology: Micrographs highlighting regional variations in vascular cell wall thickness and luminal integrity of WKY (G-I: 8, 14, and 42 weeks respectively) and SHRSP (J-L: 8, 14, and 42 weeks respectively) rats. Red arrows denote representative microvessels showing varying degrees of structural remodeling and mural thickening. M: Quantitative analysis of the presence of thick vessel wall in the hippocampus in comparison between different age groups. Each column represents the mean ± standard deviation (SD) of SHRSP and WKY rats. The results were based on a score of 1, which indicates the absence of the thick vessel wall, while 2 indicates the presence.

DG) was performed using H&E-stained sections (Fig. 6A–R). Quantitative comparisons across strain and age were analyzed using two-way ANOVA (Fig. 6S–U). No statistically significant differences were observed in the thickness of CA1, CA3, or DG across age groups or between SHRSP and WKY rats. These results indicate that gross hippocampal architecture remains largely preserved, despite the presence of vascular alterations.

3.5.3. *Neuronal viability*

Neuronal integrity was assessed using Nissl staining across hippocampal subregions (Fig. 7A–R), with quantitative analysis presented in Fig. 7S–U. In the CA1 region, no significant differences in neuronal viability were detected between strains or across age groups (Fig. 7A–F). Similarly, the DG showed no significant variation in cell viability (Fig. 7M–R). In contrast, the CA3 region exhibited a significant reduction in neuronal viability in older SHRSP rats compared to age-matched WKY controls (Fig. 7G–L), indicating region-specific vulnerability.

Taken together, these findings suggest that microvascular alterations (e.g., ePVS and vessel wall changes) occur in the absence of overt structural atrophy, while selective neuronal vulnerability emerges in specific hippocampal subregions (CA3) at later stages. This pattern supports the notion that microstructural and cellular changes may precede detectable gross morphological alterations in early-to-mid CSVD progression.

3.6. *Whole-brain and hippocampal: diffusion MRI findings*

Diffusion MRI metrics at both the whole-brain and hippocampus are presented in Table 3, with estimated marginal means visualized in Fig. 8. At the global level, FA remained relatively stable across both strain and age groups, suggesting preservation of overall white matter microstructural organization. Mixed-effects two-way ANOVA revealed no significant main effects of strain ($F\ [1,11] = 0.010$, $p = 0.921$, $\eta^2 = 0.001$) or age ($F\ [2,11] = 1.319$, $p = 0.307$, $\eta^2 = 0.193$), and no significant strain × age interaction ($F\ [2,11] = 0.483$, $p = 0.629$, $\eta^2 = 0.081$) for whole-brain FA. These findings indicate that global anisotropic integrity is largely maintained, despite the presence of vascular risk factors and ageing.

Consistent with the FA findings, whole-brain diffusivity metrics did not reveal significant effects of strain or age. MD showed no significant main effects of strain ($F\ [1,11] = 0.936$, $p = 0.354$) or age ($F\ [2, 11] = 1.611$, $p = 0.244$), and no significant interaction between factors ($F\ [2,11] = 0.315$, $p = 0.736$). Similarly, AD and RD exhibited no significant differences across groups. For AD, neither strain ($F\ [1, 11] = 0.807$, $p = 0.388$) nor age ($F\ [2,11] = 2.061$, $p = 0.174$) showed significant effects. RD followed a comparable pattern, with no significant influence of strain ($F\ [1,11] = 0.993$, $p = 0.340$) or age ($F\ [2, 11] = 1.297$, $p = 0.312$). Collectively, these findings suggest that global diffusivity measures remain largely unchanged, indicating an absence of detectable whole-brain microstructural alterations between WKY and SHRSP rats across the examined age range.

ROI analyses of the hippocampus revealed that there were no significant strain-dependent differences across all diffusion metrics (all $p > 0.25$). Furthermore, strain × age interactions remained non-significant in the hippocampus following Bonferroni correction. Collectively, these results indicate that neither chronic hypertension nor aging induced detectable hippocampal microstructural alterations within the investigated time frame, suggesting preservation of diffusion-derived structural integrity across both white and grey matter regions.

4. Discussion

The present study provides a multimodal characterization of early-to-late stage CSVD in the SHRSP rats, integrating behavioral

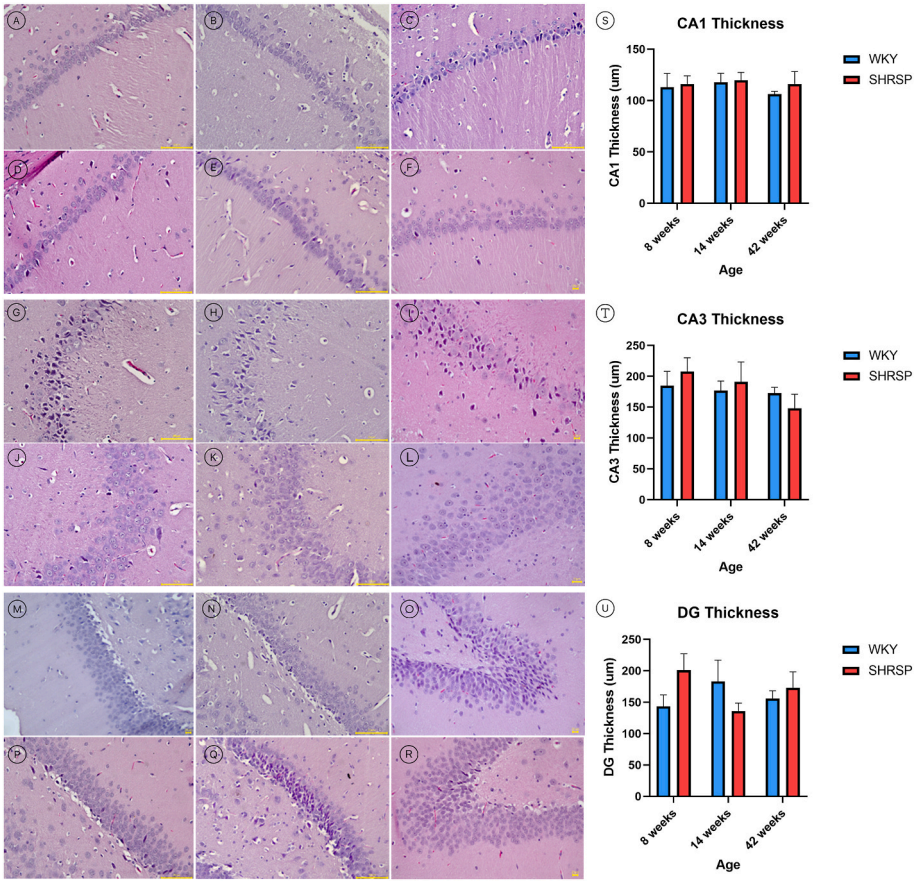

Fig. 6. Representative Hematoxylin and Eosin (H&E) staining of CA1, CA3, and dentate gyrus (DG) of the hippocampus in Wistar-Kyoto (WKY) and spontaneous hypertensive stroke-prone (SHRSP) rats. Micrographs demonstrate structural changes across age cohorts (8, 14, and 42 weeks) at 20× magnification. (A–F) CA1 regions: Longitudinal comparison showing the CA1 of WKY (A-C: 8, 14, and 42 weeks respectively) and SHRSP (D-F: A-C, 8, 14, and 42 weeks respectively) rats. (G–L) CA3 regions of WKY (G-I: 8, 14, and 42 weeks respectively) and SHRSP (J-L: A-C, 8, 14, and 42 weeks respectively) rats. (M-R) DG regions of WKY (M-O: 8, 14, and 42 weeks respectively) and SHRSP (P-R: A-C, 8, 14, and 42 weeks respectively) rats. S-U: Quantitative analysis of the CA1, CA3, and DG hippocampal thickness in comparison between different age groups. Each column represents the mean ± standard deviation (SD) of SHRSP and WKY rats.

phenotyping, diffusion MRI, and histopathological assessment across the disease trajectory. The principal finding is a clear temporal dissociation between functional impairment and structural readouts: behavioral deficits, particularly in locomotion, spatial learning, and recognition memory, emerge with advancing age in SHRSP, whereas conventional diffusion MRI metrics and gross hippocampal morphology remain largely preserved. Subtle vascular alterations (e.g., ePVS and vessel wall changes) and region-specific neuronal vulnerability (notably within hippocampal-CA3) provide a partial substrate for these deficits, but do not fully account for the magnitude of functional decline. Together, these findings suggest that behavioral impairment may emerge prior to detectable abnormalities using conventional diffusion MRI and gross morphometric measures, although this interpretation should be considered in light of the methodological sensitivity limitations of the current imaging approach.

A prerequisite for interpreting downstream findings is validation of the disease model. As expected, SHRSP rats exhibited consistently elevated SBP relative to WKY controls, confirming a hypertensive phenotype central to CSVD pathogenesis. Although age effects on SBP were not statistically significant, the persistent strain effect is consistent with the well-established role of chronic hypertension as a primary driver of small vessel remodeling, endothelial dysfunction, and BBB compromise [6,7]. The absence of strong age interaction likely reflects variability inherent to tail-cuff measurements and the known heterogeneity in blood pressure trajectories in SHRSP rats, particularly at later stages [28]. Importantly, body weight differed significantly between strains and across age, with SHRSP rats exhibiting lower weight gain, a pattern frequently reported in this model and attributed to increased metabolic demand and disease burden [29,30]. While body weight itself is not a direct CSVD marker, it may modulate physiological reserve and contribute indirectly to behavioral outcomes [27].

Behaviorally, the data suggest age-associated alterations in SHRSP rats; however, these findings should be interpreted cautiously within the context of the present physiological dataset. Although SHRSP rats demonstrated persistently elevated SBP relative to WKY controls, significant age effects and strain × age interactions were not observed for SBP measurements. Therefore, while the SHRSP model is widely recognized as a progressive model of hypertension-associated CSVD in the broader literature, the current SBP findings alone do not provide definitive evidence of progressive vascular worsening across the examined age groups. In the OFT, locomotor activity declined with age in SHRSP rats but remained stable in WKY rats. However, reduced locomotion may reflect multiple interacting factors, including motor dysfunction, systemic disease burden, altered motivation, stress responsiveness, or general physiological decline, rather than exclusively cognitive impairment or CSVD-related dysfunction [31]. Interestingly, SHRSP rats demonstrated relatively greater central zone exploration at later ages, which may reflect altered anxiety-like behavior or impaired risk assessment rather than increased exploration per se [32]. This pattern has been described in models with frontal–subcortical dysfunction, where disinhibition and impaired environmental appraisal can increase center occupancy despite reduced overall locomotion [33,34].

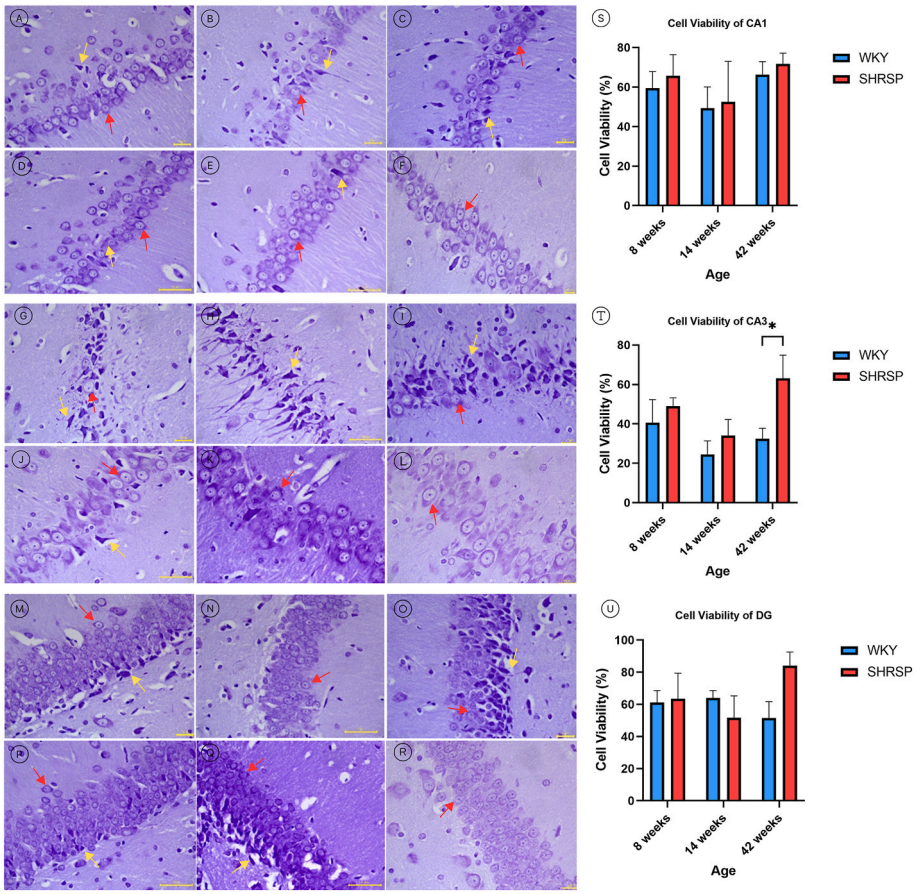

Fig. 7. Representative of Nissl staining of CA1, CA3, and dentate gyrus (DG) of the hippocampus in Wistar-Kyoto (WKY) and spontaneous hypertensive stroke-prone (SHRSP) rats. Micrographs demonstrate structural changes across age cohorts (8, 14, and 42 weeks) at 40× magnification. (A–F) CA1 regions: Longitudinal comparison showing the CA1 of WKY (A-C: 8, 14, and 42 weeks respectively) and SHRSP (D-F: A-C, 8, 14, and 42 weeks respectively) rats. (G–L) CA3 regions of WKY (G-I: 8, 14, and 42 weeks respectively) and SHRSP (J-L: A-C, 8, 14, and 42 weeks respectively) rats. (M-R) DG regions of WKY (M-O: 8, 14, and 42 weeks respectively) and SHRSP (P-R: A-C, 8, 14, and 42 weeks respectively) rats. S-U: Quantitative analysis of the CA1, CA3, and DG hippocampal cell viability in comparison between different age groups. Each column represents the mean ± standard deviation (SD) of SHRSP and WKY rats. Red arrows indicate viable cells, while yellow arrows indicate dead cells.

Table 3
Mean and standard deviation (SD) of diffusion MRI parameters across experimental groups.

Variables	Age					
	8W		14W		42W	
	WKY	SHRSP	WKY	SHRSP	WKY	SHRSP
Whole brain						
FA	0.267 ± 0.010	0.267 ± 0.010	0.267 ± 0.010	0.267 ± 0.010	0.267 ± 0.010	0.267 ± 0.010
MD	0.797 ± 0.233	0.907 ± 0.023	0.919 ± 0.055	0.947 ± 0.023	0.957 ± 0.068	0.973 ± 0.466
AD	1.026 ± 0.307	1.161 ± 0.032	1.199 ± 0.033	1.243 ± 0.032	1.245 ± 0.054	1.245 ± 0.009
RD	0.683 ± 0.196	0.781 ± 0.190	0.779 ± 0.663	0.800 ± 0.020	0.813 ± 0.075	0.837 ± 0.065
Hippocampus						
FA	0.263 ± 0.015	0.267 ± 0.005	0.279 ± 0.031	0.289 ± 0.009	0.278 ± 0.037	0.257 ± 0.037
MD	0.818 ± 0.218	0.912 ± 0.026	0.918 ± 0.056	0.970 ± 0.045	0.959 ± 0.081	0.968 ± 0.038
AD	1.050 ± 0.289	1.169 ± 0.036	1.194 ± 0.034	1.266 ± 0.061	1.247 ± 0.065	1.232 ± 0.002
RD	0.702 ± 0.183	0.784 ± 0.022	0.822 ± 0.038	0.822 ± 0.038	0.815 ± 0.089	0.836 ± 0.056

Data are presented in mean ± standard deviations (SD). WKY, Wistar Kyoto rats; SHRSP, Stroke-prone spontaneously hypertensive rats.

Recognition memory performance in SHRSP rats showed a descriptive decline at 42 weeks relative to earlier time points; however, strain × age interactions and several between-group comparisons did not reach statistical significance. Therefore, these findings should be interpreted cautiously as suggestive trends rather than definitive evidence of recognition memory impairment. A similar trajectory was observed in the MWM, where spatial learning was preserved in both strains at 8 and 14 weeks but became impaired in aged SHRSP rats, accompanied by inconsistent acquisition curves and reduced improvement across trials. Probe trial performance suggested a parallel decline in spatial memory retention. These findings are consistent with previous work demonstrating that SHRSP rats develop cognitive impairment in later stages, particularly in hippocampal-dependent domains [35,36]. Mechanistically, such deficits are often attributed to cumulative

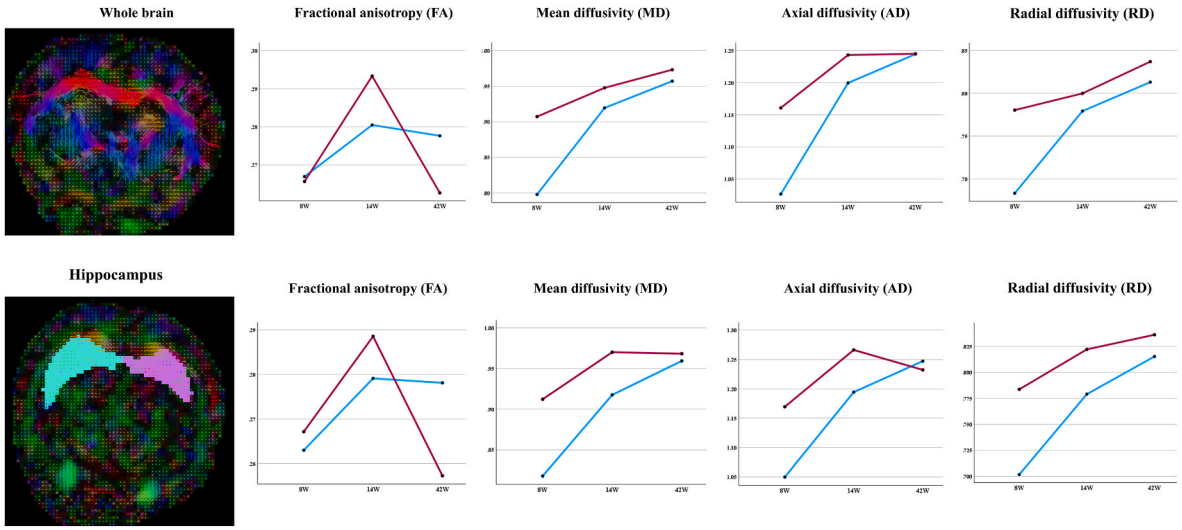

Fig. 8. Diffusion tensor imaging (DTI) parameters across the whole brain and hippocampal structures. 1st column: representative DTI maps of the whole brain and the hippocampus. Column 2 – column 4: Line graph of estimated marginal means (*y*-axis) of fractional anisotropy (FA), mean diffusivity (MD), axial diffusivity (AD), and radial diffusivity (RD) are shown for the whole brain and hippocampus in WKY (blue line) and SHRSP rats (red line) across ages (8W, 14W, and 42W) (*x*-axis). Line graphs represent estimated marginal means with corresponding 95% confidence intervals (CI) (*y*-axis).

microvascular dysfunction, reduced cerebral perfusion, and impaired neurovascular coupling, all of which can disrupt synaptic plasticity before neuronal loss becomes widespread [35].

A central and somewhat unexpected observation is the absence of significant whole-brain and hippocampal diffusion MRI alterations across strain and age. FA and diffusivity metrics (MD, AD, RD) remained stable not only globally but also within the hippocampus. At face value, this suggests preservation of microstructural integrity [37]. However, this interpretation warrants careful consideration. Conventional DTI metrics are relatively insensitive to subtle microvascular pathology, particularly in early CSVD, where changes may be confined to perivascular compartments, endothelial layers, or low-grade inflammatory processes [25]. Clinical studies have shown that DTI alterations often lag behind functional impairment and may only become evident with more advanced white matter damage, such as demyelination or axonal loss [24,38]. Moreover, the spatial resolution and signal-to-noise constraints of clinical 3T MRI adapted for small animals may limit detection of fine-scale alterations [39]. The current findings, therefore, align with an emerging view that DTI-negative CSVD does not equate to the absence of pathology but rather reflects limitations in sensitivity to early or subtle changes [26].

Histopathological analyses provide additional context, whereby ePVS were observed across all groups, suggesting that their presence alone is not sufficient to distinguish disease state in this model. While ePVS are commonly associated with impaired glymphatic clearance and vascular dysfunction, their ubiquity here may reflect baseline anatomical features or early subclinical changes [40,41]. Besides, vessel wall thickening was variably present but did not differ significantly across groups, indicating that overt structural remodeling of small vessels may not yet be pronounced or detectable with the methods employed. Notably, neither microbleeds nor hemosiderin deposition was identified within the hippocampus, consistent with the absence of overt hemorrhagic pathology at the examined stages. However, this finding should not be interpreted as evidence of a global absence of hemorrhagic involvement. In both preclinical and clinical CSVD, cerebral microbleeds exhibit a regionally heterogeneous distribution, with a predilection for subcortical and deep brain structures such as the basal ganglia, thalamus, brainstem, and deep white matter, rather than the hippocampus [42].

In SHRSP models, spontaneous hemorrhagic lesions are well documented but tend to localize preferentially to penetrating arteriolar territories and watershed regions subjected to high hemodynamic stress, where vessel wall fragility, lipohyalinosis, and fibrinoid necrosis are more pronounced [43]. Similarly, human imaging studies consistently report that hypertensive microbleeds are most frequently detected in deep and infratentorial regions, whereas hippocampal involvement is relatively uncommon unless the disease has progressed to more advanced or mixed pathologies [44]. Therefore, the absence of microbleeds and hemosiderin deposition in the hippocampus in the present study likely reflects regional vulnerability patterns rather than true disease absence. It is plausible that hemorrhagic manifestations may have developed in other brain regions not systematically assessed in the current histological analysis. This interpretation is further supported by the temporal staging of the model, as the selected time points may represent a phase characterized predominantly by vascular remodeling and functional impairment, preceding the onset of overt hemorrhagic damage. Collectively, these findings underscore the importance of region-specific evaluation in CSVD and suggest that future studies incorporating whole-brain histological mapping or susceptibility-sensitive imaging techniques (e.g., T2*-weighted MRI or susceptibility-weighted imaging) may provide a more comprehensive assessment of microbleed burden and its spatial distribution.

Moreover, despite the relative preservation of gross hippocampal architecture, neuronal assessment revealed reduced neuronal viability within the CA3 subfield in aged SHRSP rats, representing one of the more biologically meaningful positive findings in the present study. However, this observation was based on conventional Nissl staining and general morphological assessment rather than cell-type-specific, synaptic, vascular, inflammatory, or molecular characterization. The CA3 region is distinguished by its dense recurrent collateral network, which underpins pattern completion and associative memory processes but also imposes high synaptic and metabolic demand [45]. Such characteristics render CA3 neurons particularly sensitive to subtle disruptions in cerebral perfusion and oxygen delivery, conditions that are increasingly compromised in CSVD due to chronic microvascular dysfunction and impaired neurovascular coupling [46]. However, these mechanisms were not directly evaluated in the current study and should therefore be interpreted cautiously as potential explanatory hypotheses rather than definitive conclusions. In addition, CA3 is supplied by relatively delicate microvascular networks that may be more susceptible to hypertension-induced alterations, including endothelial dysfunction, reduced vasoreactivity, and BBB perturbation. These vascular changes

can precipitate a state of chronic, low-grade hypoperfusion, which has been shown to preferentially affect metabolically demanding neuronal populations [47]. Experimental and clinical studies have similarly reported that CA3 exhibits early synaptic and dendritic alterations under conditions of vascular insufficiency, even in the absence of overt neuronal loss or volumetric atrophy [48,49]. Similarly, while ePVS were consistently observed, their presence across all experimental groups limits their specificity as a disease-associated marker within this dataset. In addition, the absence of hippocampal microbleeds and hemosiderin deposition does not exclude vascular pathology in other brain regions but instead reflects the regional scope of the present histological sampling. Consequently, broader whole-brain histological mapping and multimodal vascular characterization will be necessary in future studies to more comprehensively define the spatial and mechanistic landscape of CSVD pathology.

The absence of comparable changes in CA1 and the DG further supports the notion that neurodegeneration in CSVD is spatially heterogeneous rather than diffuse. While CA1 is traditionally considered highly vulnerable to acute ischemic insults, it may be relatively preserved under conditions of chronic, moderate hypoperfusion, whereas CA3 appears more sensitive to sustained microvascular stress and network-level dysfunction [49]. The DG, with its distinct neurogenic niche and different vascular architecture, may also exhibit greater resilience at this stage of disease progression. Importantly, the emergence of CA3-specific neuronal compromise coincides with the observed decline in recognition memory and spatial learning, reinforcing the functional relevance of this subfield. Crucially, these cellular alterations occur in the absence of detectable changes in hippocampal thickness or diffusion MRI indices, highlighting a disconnect between microstructural integrity and functional performance. This supports the concept that early CSVD-related cognitive impairment is driven by subtle cellular and circuit-level dysfunction that precedes overt structural degeneration detectable by conventional imaging or morphometric analysis [50].

Taken together, the present findings indicate that selected behavioral alterations and limited regional histopathological abnormalities were detectable despite the absence of significant abnormalities using conventional diffusion MRI metrics and gross morphometric assessments. Importantly, several behavioral outcomes, particularly within the NOR and portions of the MWM analyses, remained descriptive and should therefore be interpreted cautiously. Prior literature suggests that microvascular dysfunction may contribute to impaired neurovascular coupling, subtle microstructural alterations within normal-appearing white matter, and reduced efficiency of large-scale brain networks, all of which have been associated with cognitive impairment in CSVD, even when conventional MRI lesion burden appears modest [51,52]. However, these mechanisms were not directly evaluated in the current study and should therefore be interpreted as potential explanatory hypotheses rather than conclusions directly supported by the present data. Consequently, the current findings do not provide definitive evidence that early CSVD-related microstructural dysfunction precedes detectable imaging abnormalities. Rather, the data suggests that subtle behavioral and cellular alterations may occur in parallel with negative conventional DTI findings within the sensitivity limits of the employed imaging framework.

Notably, the coexistence of preserved diffusion MRI metrics with subtle behavioral and histological abnormalities may itself represent a potentially relevant translational observation in early-stage CSVD. Conventional diffusion metrics derived from standard tensor models may lack sufficient sensitivity to detect subtle vascular, perivascular, inflammatory, or cellular alterations occurring during early disease progression. Therefore, further studies incorporating advanced multimodal imaging, connectomics, perfusion assessment, BBB evaluation, and molecular analyses are required to clarify the underlying mechanisms and better define the earliest pathological stages of CSVD.

4.1. Limitations and future directions

Several limitations warrant careful consideration when interpreting the present findings. First, although the use of a clinical 3T MRI system enhances translational relevance, it inherently limits spatial resolution and sensitivity compared to dedicated high-field preclinical systems, and may therefore underestimate subtle microstructural alterations, particularly within small or heterogeneous regions [53]. Second, diffusion MRI analyses were restricted to conventional tensor-derived metrics. While widely used, these parameters lack specificity to disentangle complex microstructural changes; more advanced approaches such as neurite orientation dispersion and density imaging (NODDI), free-water imaging, or multi-compartment diffusion models may offer greater sensitivity to early CSVD-related pathology [54]. Besides, future investigations incorporating susceptibility-sensitive imaging modalities such as susceptibility-weighted imaging (SWI/SWAN) and high-resolution T2/T2*-weighted MRI may improve the detection of cerebral microbleeds, hemosiderin deposition, and subtle vascular abnormalities associated with CSVD.

Importantly, the relatively limited spatial resolution and voxel size achievable using a clinical 3T MRI platform for small-animal imaging may increase susceptibility to partial volume effects, particularly within anatomically small and heterogeneous structures such as hippocampal subfields. Consequently, subtle microvascular, perivascular, inflammatory, or cellular alterations may remain below the detection threshold of conventional tensor-derived diffusion metrics. Therefore, the absence of significant diffusion abnormalities in the present study should be interpreted as the absence of detectable alterations within the sensitivity limits of the employed imaging framework, rather than definitive evidence of preserved microstructural integrity.

Another limitation is that the ROI focuses on the hippocampus, which, while justified by its role in cognition, does not fully capture the diffuse and whole-brain nature of CSVD. Small vessel pathology affects widespread vascular territories, particularly deep white matter, subcortical nuclei, and cortical–subcortical networks [23]. Consequently, restricting analyses to the hippocampus may overlook critical alterations in other vulnerable regions such as the corpus callosum, internal capsule, thalamus, and frontal-subcortical circuits. Future studies should therefore adopt a more comprehensive, whole-brain ROI framework, complemented by connectome-based analyses, to better characterize network-level disruptions. Structural and functional connectomics could provide critical insight into how distributed microvascular injury translates into large-scale network inefficiency and cognitive decline, potentially revealing alterations that are not detectable using regional or voxel-wise approaches alone [55].

Although the observed reduction in neuronal viability within the CA3 subfield represents one of the more biologically meaningful findings of the present study, its interpretation remains constrained by methodological limitations. Histological evaluation was limited primarily to conventional H&E and Nissl staining, which provides largely morphological and descriptive information regarding vascular architecture and neuronal integrity. While these approaches enabled identification of structural abnormalities such as ePVS, vessel wall alterations, and reduced neuronal viability, they do not permit definitive mechanistic characterization of the underlying biological processes. Consequently, interpretations related to microvascular dysfunction, neuronal vulnerability, cellular dysfunction, neuroinflammation, impaired neurovascular coupling, or selective CA3 susceptibility should be considered cautiously and viewed as potential explanatory hypotheses rather than conclusions directly established by the present data. Importantly, the study did not include immunohistochemical or molecular analyses to assess endothelial integrity, BBB permeability, inflammatory signaling, glial activation, synaptic alterations, oxidative stress, apoptosis-related pathways, or vascular remodeling.

In addition, stereological approaches were not employed, which may limit the precision and robustness of regional neuronal quantification.

Therefore, the biological specificity and functional significance of the reported CA3 alterations remain difficult to fully establish within the context of the present dataset. Future studies incorporating cell-type-specific neuronal and glial markers, BBB assessment, vascular and inflammatory profiling, apoptosis-related analyses, synaptic characterization, stereological quantification, and molecular validation techniques will be necessary to better define the mechanistic basis of the observed structural and behavioral alterations in early-stage CSVD and to determine whether the observed CA3 changes reflect true neurodegenerative processes, altered neuronal metabolism, inflammatory responses, synaptic remodeling, or other cellular mechanisms associated with disease progression.

Next, the cross-sectional design restricts the ability to infer temporal dynamics within individual animals. Longitudinal studies are needed to map the sequence of events linking vascular dysfunction, neuronal compromise, and behavioral decline. Additionally, variability in physiological measures such as SBP may have reduced sensitivity to detect age-dependent effects, particularly given the known heterogeneity of the SHRSP phenotype. Moreover, although age-based grouping was employed to examine different stages of disease vulnerability within the SHRSP model, significant age-dependent progression in SBP was not observed in the present dataset. Consequently, interpretations regarding progressive vascular deterioration should not be based solely on the current physiological measurements. Nevertheless, the broader validity of SHRSP as a progressive preclinical model of hypertension-associated CSVD remains well established in prior experimental literature.

Finally, although behavioral paradigms were carefully implemented, performance outcomes may be influenced by non-cognitive factors, including motivation, visual acuity, and stress responsiveness, which are known to change with aging and disease progression [56]. Future investigations should prioritize multimodal, longitudinal, and system-level approaches to more fully characterize CSVD pathophysiology. The integration of high-field MRI, advanced diffusion modeling, and susceptibility-based imaging could improve the detection of microstructural and microvascular abnormalities. Expanding analyses beyond single regions to include whole-brain network architecture and connectome organization will be essential to understanding how localized vascular pathology propagates into global functional impairment. In parallel, incorporation of molecular, cellular, and fluid biomarkers will provide mechanistic depth and facilitate translation to human studies. Ultimately, combining these approaches with early-stage therapeutic interventions may help determine whether the functional deficits observed in preclinical CSVD are reversible before irreversible structural damage occurs.

5. Conclusion

This study demonstrates that age-related behavioral impairment in SHRSP rats can occur in the absence of detectable abnormalities using conventional diffusion MRI metrics and gross hippocampal morphometry within the sensitivity limits of the current experimental framework. Age-dependent alterations in locomotor activity were observed in SHRSP rats, while recognition memory and spatial learning assessments demonstrated more modest or descriptive behavioral differences that should be interpreted cautiously, given the limited statistical significance of several comparisons, despite largely preserved diffusion MRI indices and gross hippocampal morphology. Histopathological analyses revealed subtle vascular alterations and selective neuronal vulnerability within the CA3 subfield, indicating that early CSVD is characterized by regional and cellular perturbations rather than widespread degeneration. These findings highlight the possibility that behavioral impairment may be detectable before abnormalities become evident using conventional structural imaging approaches, although further multimodal and mechanistic investigations are required to determine the biological basis of this apparent divergence. Taken together, this work positions early CSVD as a clinically silent but biologically active phase, where intervention may still be feasible before irreversible damage occurs. Advancing toward multimodal, whole-brain, and connectome-based frameworks, alongside integration of molecular biomarkers, will be necessary to clarify the mechanisms underlying this apparent divergence.

Ethical approval

All experimental procedures were conducted in accordance with the guidelines of the Institutional Animal Care and Use Committee (IACUC), Universiti Putra Malaysia (UPM), under approved protocol number UPM/IACUC/AUP-R004/2021.

Statement for studies on humans/animals

This study uses animal models (rats).

Funding statement

This study was supported by the Ministry of Higher Education (MOHE) Malaysia under the Fundamental Research Grant Scheme (FRGS) [FRGS/1/2019/SKK08/UPM/02/5].

CRediT authorship contribution statement

Che Mohd Nasril Che Mohd Nassir: Data curation, Formal analysis, Validation, Writing – original draft. **Hafizah Abdul Hamid:** Conceptualization, Data curation, Formal analysis, Funding acquisition, Investigation, Methodology, Project administration, Supervision, Validation, Writing – review & editing. **Nurfatihah Pahdin:** Formal analysis, Investigation, Writing – review & editing. **Izzatul Farhanis Abdul Halim:** Formal analysis, Investigation, Writing – review & editing. **Laurasharwini Sivakumar:** Formal analysis, Investigation, Writing – review & editing. **Mohd Khairi Hussain:** Resources, Writing – review & editing. **Tengku Azam Shah Tengku Mohamad:** Resources, Writing – review & editing. **Zaw Myo Hein:** Validation, Writing – review & editing. **Muhammad Zulfadli Mehat:** Investigation, Validation, Writing – review & editing.

Declaration of competing interest

The authors declare no conflict of interest.

Acknowledgments

We sincerely thank the research and laboratory staff for their dedication and support throughout the study. The authors would also like to acknowledge that the assistance of ChatGPT 5.0, an AI language model developed by OpenAI, was used to help in the refinement of certain limited sections of this manuscript, particularly for the language editing. Further, all AI-assisted content has been duly reviewed and thoroughly edited by the authors to ensure accuracy, scientific rigor, and adherence to the standards of academic writing. Authors are fully responsible for the content of this manuscript, even those parts improved by an AI tool, and are thus liable for any breach of publication ethics.

Data availability

We declare that all data supporting the findings of this study are available upon request to the corresponding authors.

References

[1] Q. Li, Y. Yang, C. Reis, T. Tao, W. Li, X. Li, J.H. Zhang, Cerebral small vessel disease, Cell Transplant. 27 (12) (2018) 1711–1722, https://doi.org/10.1177/0963689718795148.

[2] H. Huang, W. Song, P. Wang, Y. Zhu, L. Zheng, C. Shen, H. Xu, J. Qiu, White matter hyperintensities: cerebral small-vessel diseases and white matter microstructural impairments, iRADIOLOGY 3 (2025) 5–25, https://doi.org/10.1002/ird3.121.
[3] J. Litak, M. Mazurek, B. Kulesza, P. Szmygin, J. Litak, P. Kamieniak, C. Grochowski, Cerebral small vessel disease, Int. J. Mol. Sci. 21 (24) (2020) 9729, https://doi.org/10.3390/ijms21249729.
[4] N. Dupré, A. Drieu, A. Joutel, Pathophysiology of cerebral small vessel disease: a journey through recent discoveries, J. Clin. Investig. 134 (10) (2024) e172841, https://doi.org/10.1172/JCI172841.
[5] Y. Inoue, F. Shue, G. Bu, et al., Pathophysiology and probable etiology of cerebral small vessel disease in vascular dementia and Alzheimer's disease, Mol. Neurodegener. 18 (46) (2023), https://doi.org/10.1186/s13024-023-00640-5.
[6] Y. Hannawi, E. Caceres, M.G. Ewees, K.A. Powell, A. Bratasz, J.M. Schwab, C. L. Rink, J.L. Zweier, Characterizing the neuroimaging and histopathological correlates of cerebral small vessel disease in spontaneously hypertensive stroke-prone rats, Front. Neurol. 12 (2021) 740298, https://doi.org/10.3389/fneur.2021.740298.
[7] M. Wu, D. Li, F. Qiu, H. Nie, R. Fang, Z. Zhong, H. Yang, X. Lin, X. Wang, H. Wen, L. Gong, P. Meng, Aging aggravates cognitive dysfunction in spontaneously hypertensive rats by inducing cerebral microvascular endothelial dysfunction, PLoS One 20 (3) (2025) e0316383, https://doi.org/10.1371/journal.pone.0316383.
[8] H.R. Ismawi, K. Zulkiflee, Y.S. Yusoff Azmi Merican, M. Mohd Zainudin, A. Abd Fuaat, F. Zainal Abidin, Vascular ultrastructural changes in hypertensive rodent models: a 15-Year scoping review, Malaysian J. Med. Health Sci. 21 (5) (2025) 302–309, https://doi.org/10.47836/mjmhs.21.5.33.
[9] E.N. Bakker, G. Groma, L.J. Spijkers, J. de Vos, A. van Weert, H. van Veen, V. Everts, S.M. Arribas, E. VanBavel, Heterogeneity in arterial remodeling among sublines of spontaneously hypertensive rats, PLoS One 9 (9) (2014) e107998, https://doi.org/10.1371/journal.pone.0107998.
[10] M.M.A. Bouwman, I. Frigerio, C.P. Lin, N. Reijner, W.D.J. van de Berg, L. E. Jonkman, Hippocampal subfields: volume, neuropathological vulnerability and cognitive decline in Alzheimer's and Parkinson's disease, Alzheimers Res. Ther. 17 (1) (2025) 121, https://doi.org/10.1186/s13195-025-01768-w.
[11] A.-M. Einenkel, A. Salameh, Selective vulnerability of hippocampal CA1 and CA3 pyramidal cells: what are possible pathomechanisms and should more attention be paid to the CA3 region in future studies? J. Neurosci. Res. 102 (2023) e25276 https://doi.org/10.1002/jnr.25276.
[12] S.J. van Veluw, K. Arfanakis, J.A. Schneider, Neuropathology of vascular brain health: insights from Ex vivo magnetic resonance imaging-histopathology studies in cerebral small vessel disease, Stroke 53 (2) (2022) 404–415, https://doi.org/10.1161/STROKEAHA.121.032608.
[13] H. Abdul Hamid, A. Hambali, U. Okon, C.M.N. Che Mohd Nassir, M.Z. Mehat, A. Norazit, M. Mustapha, Is cerebral small vessel disease a central nervous system interstitial fluidopathy? IBRO Neurosci. Rep. 16 (2023) 98–105, https://doi.org/10.1016/j.ibneur.2023.12.004.
[14] V. Zvenigorodsky, B.F. Gruenbaum, I. Shelef, D. Frank, B. Tsafarov, S. Negev, V. Zeldetz, A.N. Azab, M. Boyko, A. Zlotnik, Sensitivity of diffusion tensor imaging for assessing injury severity in a rat model of isolated diffuse axonal injury: Comparison with histology and neurological assessment, Int. J. Mol. Sci. 26 (15) (2025) 7333, https://doi.org/10.3390/ijms26157333.
[15] B. Tornifoglio, A.J. Stone, R.D. Johnston, et al., Diffusion tensor imaging and arterial tissue: establishing the influence of arterial tissue microstructure on fractional anisotropy, mean diffusivity and tractography, Sci. Rep. 10 (2020) 20718, https://doi.org/10.1038/s41598-020-77675-x.
[16] A.C. Johnson, Hippocampal vascular supply and its role in vascular cognitive impairment, Stroke 54 (3) (2023) 673–685, https://doi.org/10.1161/STROKEAHA.122.038263.
[17] D.N. Abrous, N. Blin, C.J. Boraxbekk, G. Catheline, C.P. Fitzsimons, M. Hilscher, M. Lemoine, L.V. Lopes, A. Maass, M. Nilsson, L. Nyberg, L.J. Rassmussen, M. Remondes, M. Sauvage, S. Schreiber, T. Wolbers, Hallmarks of healthy cognitive aging: inter-individual differences in aging trajectories, Ageing Res. Rev. (2026) 103102, https://doi.org/10.1016/j.arr.2026.103102. Advance online publication.
[18] Z. Firdaus, N. Singh, S.K. Prajapati, et al., Centella Asiatica prevents D-galactose-Induced cognitive deficits, oxidative stress and neurodegeneration in the adult rat brain, Drug Chem. Toxicol. 45 (2022) 1417–1426, https://doi.org/10.1080/01480545.2020.1833907.
[19] S.M. Chiroma, M.T. Hidayat Baharuldin, Mat Taib Cn, et al., Protective effect of Centella Asiatica against D -galactose and aluminium chloride induced rats: behavioral and ultrastructural approaches, Biomed. Pharmacother. 109 (2019) 853–864, https://doi.org/10.1016/j.biopha.2018.10.111.
[20] M. Giorgetti, J.A. Gibbons, S. Bernales, I.E. Alfaro, C. Drieu La Rochelle, T. Cremers, C.A. Altar, R. Wronski, B. Hutter-Paier, A.A. Protter, Cognition-enhancing properties of Dimebon in a rat novel object recognition task are unlikely to be associated with acetylcholinesterase inhibition or N-methyl-D-aspartate receptor antagonism, J. Pharmacol. Exp. Therapeut. 333 (3) (2010) 748–757, https://doi.org/10.1124/jpet.109.164491.
[21] F.C. Yeh, DSI studio: an integrated tractography platform and fiber data hub for accelerating brain research, Nat. Methods 22 (8) (2025) 1617–1619, https://doi.org/10.1038/s41592-025-02762-8.
[22] F.C. Yeh, T.D. Verstynen, Y. Wang, J.C. Fernández-Miranda, W.Y. Tseng, Deterministic diffusion fiber tracking improved by quantitative anisotropy, PLoS One 8 (11) (2013) e80713, https://doi.org/10.1371/journal.pone.0080713.
[23] A.H. Hainsworth, H.S. Markus, J.A. Schneider, Cerebral small vessel disease, hypertension, and vascular contributions to cognitive impairment and dementia, Hypertension 81 (1) (2024) 75–86, https://doi.org/10.1161/HYPERTENSIONAHA.123.19943. Dallas, Tex. : 1979.
[24] Z. Li, Y. Mei, L. Wang, et al., White matter and cortical gray matter microstructural alterations in migraine: a NODDI and DTI analysis, J. Headache Pain 26 (2025) 115, https://doi.org/10.1186/s10194-025-02059-3.
[25] J.N. Acosta, S.P. Haider, C. Rivier, A.C. Leasure, K.N. Sheth, G.J. Falcone, S. Payabvash, Blood pressure-related white matter microstructural disintegrity and associated cognitive function impairment in asymptomatic adults, Stroke Vascul. Neurol. 8 (5) (2023) 358–367, https://doi.org/10.1136/svn-2022-001929.
[26] S. Yang, Y. Zhou, F. Wang, X. He, X. Cui, S. Cai, X. Zhu, D. Wang, Diffusion tensor imaging in cerebral small vessel disease applications: opportunities and challenges, Front. Neurosci. 18 (2024) 1473462, https://doi.org/10.3389/fnins.2024.1473462.
[27] P.H. Croll, D. Bos, M.A. Ikram, F. Rivadeneira, T. Voortman, M.W. Vernooij, Body composition is not related to structural or vascular brain changes, Front. Neurol. 10 (2019) 559, https://doi.org/10.3389/fneur.2019.00559.
[28] K.J. Bigiarelli, Rodent thermoregulation: considerations for tail-cuff blood pressure measurements, JAALAS: JAALAS 61 (5) (2022) 406–411, https://doi.org/10.30802/AALAS-JAALAS-22-000006.
[29] S. Hojná, L. Mráziková, A. Shánělová, H. Pelantová, A. Montezano, R.M. Touyz, L. Maletínská, J. Kuneš, Oxidative stress, metabolic impairment, and neuroinflammation are associated with target organ damage in SHRSP, Physiol. Res. 74 (5) (2025) 779–795, https://doi.org/10.33549/physiolres.935659.
[30] M.F.P. Gomes, M.E. Borges, V.A. Rossi, E.O.C. Moura, A. Medeiros, The effect of physical resistance training on baroreflex sensitivity of hypertensive rats, Arq. Bras. Cardiol. 108 (6) (2017) 539–545, https://doi.org/10.5935/abc.20170065.
[31] Y.L. Hsieh, C.C. Yang, Age-series characteristics of locomotor activities in spontaneously hypertensive rats: a comparison with the Wistar-Kyoto strain, Physiol. Behav. 93 (4–5) (2008) 777–782, https://doi.org/10.1016/j.physbeh.2007.11.032.
[32] D.I. Mamedova, O.A. Nedogreeva, A.O. Manolova, V.O. Ovchinnikova, P. A. Kostryukov, N.A. Lazareva, Y.V. Moiseeva, L.V. Tret'yakova, A.A. Kvichansky, M.V. Onufriev, V.A. Aniol, M.R. Novikova, N.V. Gulyaeva, M.Y. Stepanichev, The impact of long-term isolation on anxiety, depressive-like and social behavior in aging Wistar-Kyoto (WKY) and spontaneously hypertensive (SHR) male rats, Sci. Rep. 14 (1) (2024) 28135, https://doi.org/10.1038/s41598-024-79677-5.
[33] M. Moya, L. López-Valencia, B. García-Bueno, L. Orio, Disinhibition-like behavior correlates with frontal cortex damage in an animal model of chronic alcohol consumption and thiamine deficiency, Biomedicines 10 (2) (2022) 260, https://doi.org/10.3390/biomedicines10020260.
[34] T. Bast, M. Pezze, S. McGarrity, Cognitive deficits caused by prefrontal cortical and hippocampal neural disinhibition, Br. J. Pharmacol. 174 (19) (2017) 3211–3225, https://doi.org/10.1111/bph.13850.
[35] A.C. Johnson, J.E. Miller, M.J. Cipolla, Memory impairment in spontaneously hypertensive rats is associated with hippocampal hypoperfusion and hippocampal vascular dysfunction, J. Cerebr. Blood Flow Metabol.: Off. J. Int. Soc. Cerebral Blood Flow Metabol. 40 (4) (2020) 845–859, https://doi.org/10.1177/0271678X19848510.
[36] P. Arndt, L. Morton, M. Briese, N. Lämmlin, H. Mattern, M. Hasanuzzaman, M. Westhues, M. Khoshneviszadeh, S. Appenzeller, D. Gündel, M. Toussaint, P. Brust, T. Kniess, A. Oelschlegel, J. Goldschmidt, S. Meuth, P. Müller, R. Braun-Dullaeus, G. Debska-Vielhaber, S. Vielhaber, S. Schreiber, Vascular and neural transcriptomics reveal stage-dependent pathways to inflammation and cognitive dysfunction in a rat model of hypertension, J. Am. Heart Assoc. 15 (6) (2026) e040710, https://doi.org/10.1161/JAHA.125.040710.
[37] R.K. Rajan, A comprehensive review on adaptive plasticity and recovery mechanisms post-acquired brain injury, Neuroprotection 3 (2025) 226–252, https://doi.org/10.1002/nep3.70006.
[38] R. Stephen, A. Solomon, T. Ngandu, E. Levälahti, J.O. Rinne, N. Kemppainen, R. Parkkola, R. Antikainen, T. Strandberg, M. Kivipelto, H. Soininen, Y. Liu, FINGER study group, White matter changes on diffusion tensor imaging in the FINGER randomized controlled trial, J. Alzheimers Dis.: JAD 78 (1) (2020) 75–86, https://doi.org/10.3233/JAD-200423.
[39] K.H. Herrmann, S. Schmidt, A. Kretz, R. Haenold, I. Krumbein, M. Metzler, C. Gaser, O.W. Witte, J.R. Reichenbach, Possibilities and limitations for high resolution small animal MRI on a clinical whole-body 3T scanner, Magma 25 (3) (2012) 233–244, https://doi.org/10.1007/s10334-011-0284-5.
[40] J. Zhang, S. Liu, Y. Wu, Z. Tang, Y. Wu, Y. Qi, F. Dong, Y. Wang, Enlarged perivascular space and index for diffusivity along the perivascular space as emerging neuroimaging biomarkers of neurological diseases, Cell. Mol. Neurobiol. 44 (1) (2023) 14, https://doi.org/10.1007/s10571-023-01440-7.
[41] Z.M. Hein, C.M.N. Che Mohd Nassir, Perivascular pathology, not macrovascular complexity, governs glymphatic-related dysfunction in preclinical cerebral small vessel disease, Sci. Rep. 16 (1) (2026) 4528, https://doi.org/10.1038/s41598-026-36001-7.
[42] Y.F. Chen, C.H. Chen, W.C. Wu, B.C. Lee, H.H. Tsai, S.C. Tang, Spatial distribution of cerebral microbleeds reveals heterogeneous pathogenesis in CADASIL, Eur. Radiol. 32 (3) (2022) 1951–1958, https://doi.org/10.1007/s00330-021-08288-9.
[43] Y. Hannawi, E. Caceres, M.G. Ewees, K.A. Powell, A. Bratasz, J.M. Schwab, C. L. Rink, J.L. Zweier, Characterizing the neuroimaging and histopathological correlates of cerebral small vessel disease in spontaneously hypertensive stroke-prone rats, Front. Neurol. 12 (2021) 740298, https://doi.org/10.3389/fneur.2021.740298.
[44] R. Pallapothu, S. Kudaravalli, R.D. Newman-Norlund, et al., Infratentorial cerebral microbleeds and brain age gap in stroke patients: a cross-sectional neuroimaging study, GeroScience (2026), https://doi.org/10.1007/s11357-026-02218-7.

[45] E. Cherubini, R. Miles, The CA3 region of the hippocampus: how is it? What is it for? How does it do it? Front. Cell. Neurosci. 9 (2015) 19, https://doi.org/10.3389/fncel.2015.00019.
[46] A. Hencz, A. Magony, C. Thomas, K. Kovacs, G. Szilagyi, J. Pal, A. Sik, Mild hypoxia-induced structural and functional changes of the hippocampal network, Front. Cell. Neurosci. 17 (2023) 1277375, https://doi.org/10.3389/fncel.2023.1277375.
[47] D. Lana, F. Ugolini, M.G. Giovannini, An overview on the differential interplay among neurons-astrocytes-microglia in CA1 and CA3 Hippocampus in Hypoxia/Ischemia, Front. Cell. Neurosci. 14 (2020) 585833, https://doi.org/10.3389/fncel.2020.585833.
[48] X. Hu, Z. Guo, Z. Shi, P. Zhen, M. Zhou, Morphological changes in CA3 pyramidal neurons after transient global ischemia, Neuroreport 36 (14) (2025) 856–863, https://doi.org/10.1097/WNR.0000000000002206.
[49] D. Jappy, R. Sokolov, Y. Dobryakova, V. Krut', K. Maltseva, A. Fedulina, I. Smirnov, A. Rozov, Early-life stress differentially affects CA3 synaptic inputs converging on apical and basal dendrites of CA1 pyramidal neurons, Front. Neural Circ. 19 (2025) 1533791, https://doi.org/10.3389/fncir.2025.1533791.
[50] X. Jia, Y. Li, X. Jia, Q. Yang, Structural network disruption of corticothalamic pathways in cerebral small vessel disease, Brain Imag. Behav. 18 (5) (2024) 979–988, https://doi.org/10.1007/s11682-024-00889-4.
[51] M. Bergamino, M.R. Nelson, E. Keeling, A.M. Stokes, Alzheimer's Disease Neuroimaging Initiative, Assessment of microstructural changes in white matter hyperintensities in aging and mild cognitive impairment revealed by advanced diffusion MRI, J. Alzheimer's Dis. Rep. 9 (2025) 25424823251395938, https://doi.org/10.1177/25424823251395938.
[52] W. Khan, M.S. Khlif, R. Mito, T. Dhollander, A. Brodtmann, Investigating the microstructural properties of normal-appearing white matter (NAWM) preceding conversion to white matter hyperintensities (WMHs) in stroke survivors, Neuroimage 232 (2021) 117839, https://doi.org/10.1016/j.neuroimage.2021.117839.
[53] S. Saito, J. Ueda, Preclinical magnetic resonance imaging and spectroscopy in the fields of radiological technology, medical physics, and radiology, Radiol. Phys. Technol. 17 (2024) 47–59, https://doi.org/10.1007/s12194-024-00785-y.
[54] P. McCunn, X. Xu, A. Moszczynski, A. Li, A. Brown, R. Bartha, Neurite orientation dispersion and density imaging in a rodent model of acute mild traumatic brain injury, J. Neuroimaging: Off. J. Am. Soc. Neuroimag. 31 (5) (2021) 879–892, https://doi.org/10.1111/jon.12917.
[55] H. Xin, C. Liang, Y. Fu, M. Feng, S. Wang, Y. Gao, C. Sui, N. Zhang, L. Guo, H. Wen, Disrupted brain structural networks associated with depression and cognitive dysfunction in cerebral small vessel disease with microbleeds, Prog. Neuro Psychopharmacol. Biol. Psychiatr. 131 (2024) 110944, https://doi.org/10.1016/j.pnpbp.2024.110944.
[56] A. Runk, Y. Jia, A. Liu, C.H. Chang, M. Ganguli, B.E. Snitz, Associations between visual acuity and cognitive decline in older adulthood: a 9-Year longitudinal study, J. Int. Neuropsychol. Soc.: JINS 29 (1) (2023) 1–11, https://doi.org/10.1017/S1355617721001363.